Regionalized regulation of actomyosin organization influences cardiomyocyte cell shape changes during chamber curvature formation

Dena M. Leerberg[1], Gabriel B. Avillion[1], Rashmi Priya[2], Didier Y.R. Stainier[2], and Deborah Yelon[1*]

[1]Department of Cell and Developmental Biology, School of Biological Sciences, University of California, San Diego, La Jolla, CA, 92093, USA.

[2]Department of Developmental Genetics, Max Planck Institute for Heart and Lung Research, Bad Nauheim, 61231, Germany.

*Correspondence to Deborah Yelon, dyelon@ucsd.edu

Abstract

Cardiac chambers emerge from a heart tube that balloons and bends to create expanded ventricular and atrial structures, each containing a convex outer curvature (OC) and a recessed inner curvature (IC). A comprehensive understanding of the cellular and molecular mechanisms underlying the formation of these characteristic curvatures remains lacking. Here, we demonstrate in zebrafish that the initially similar populations of OC and IC ventricular cardiomyocytes diverge in the organization of their actomyosin cytoskeleton and subsequently acquire distinct OC and IC cell shapes. Altering actomyosin dynamics hinders cell shape changes in the OC, and mosaic analyses indicate that actomyosin regulates cardiomyocyte shape in a cell-autonomous manner. Additionally, both blood flow and the transcription factor Tbx5a influence the basal enrichment of actomyosin and squamous cell morphologies in the OC. Together, our findings demonstrate that intrinsic and extrinsic factors intersect to control actomyosin organization in OC cardiomyocytes, which in turn promotes the cell shape changes that drive curvature morphogenesis.

Introduction

Organs are replete with curvature, from the branching distal tips of the lung epithelium to the concave cup of the retina, and to the gyri and sulci of the brain. Essentially every organ will exhibit some degree of curvature during its morphogenesis, and the precise curvature geometry required for a particular organ's function is likely sculpted from inputs both extrinsic and intrinsic to its tissues (*1*). Decades of interest in this topic show us that some curvatures rely heavily on external influences. For example, the vertebrate gut acquires its dramatic twists and turns due to its rapid lengthening combined with its restrictive attachment to a relatively static partner, the dorsal mesentery (*2*). By contrast, the ingressing *Drosophila* ventral furrow is controlled largely by tissue-intrinsic processes, with apical constriction driven by actomyosin pulses in the epithelial cells resulting in robust invagination (*3–5*). Here, we investigate the factors, both tissue-extrinsic and -intrinsic, that contribute to chamber curvature formation in the developing heart.

The heart begins as a simple tube but then transforms into a S-shaped organ with ventricular and atrial chambers. This process, generally referred to as looping, involves the bending and ballooning of the myocardial tissue to form the chambers, the twisting of the heart into a slightly helical shape (known as torsion), and the asymmetric displacement of the ventricle and atrium to deliver the chambers to their ultimate positions (*6–10*). During formation of the chambers, each acquires a bulging outer curvature (OC) and a recessed inner curvature (IC) (Fig. 1C) (*11–13*). In addition to distinctive tissue morphology, these curvatures exhibit disparate physiological features; for example, the OC exhibits higher conduction velocity (*14–16*) and more trabeculation (*17–19*) than the IC, whereas the IC demonstrates greater tissue stiffness (*20*). While the differences between the OC and IC have been well characterized, the mechanisms that initially identify these regions and control their subsequent morphogenesis and specialization remain enigmatic.

Existing lines of experimental and modeling evidence propose cell behaviors such as hypertrophic growth, rearrangement within the tissue, and changes to cell shape as potential contributors to chamber curvature morphogenesis. For example, in chick, localized increases to cardiomyocyte volume in the OC appear to play a significant role in the creation of the ventricular bend (*21*, *22*). Additionally, in both chick and zebrafish, differing cell rearrangement patterns between the curvatures (*9*, *23*), as well as regionalized cell shape changes (*24*, *25*),

likely play into the pronounced expansion of the OC tissue. In zebrafish in particular, the strikingly divergent morphologies that ventricular OC and IC cardiomyocytes attain during curvature formation have suggested that active cell shape change is a critical driver of curvature formation. Specifically, examination of the myocardial surface of the zebrafish heart tube has highlighted that its cells are fairly uniform in both apical surface area and circularity (*25*). However, after curvature formation, OC cells have a significantly larger, more elongated apical surface area than do IC cells (*25*). Consistent with the idea that regionalized cell shape changes create chamber curvatures, many mutations that cause chamber dysmorphia also disrupt the acquisition of OC- or IC-linked cell shapes (*14*, *26–30*). However, the subcellular mechanisms that drive these changes to cardiomyocyte morphology have not been well-defined.

The actomyosin cytoskeleton is an attractive candidate for mediating cell shape change. Although capable of inducing shape change in several ways, the network is perhaps best known for its ability to contract and thus create localized tension within a cell, as in the apical constriction observed during *Drosophila* ventral furrow formation (*5*, *31*). This type of actomyosin-derived tension is indeed employed at later stages of zebrafish cardiac morphogenesis, when differential tensions between cardiomyocytes are important for the decision to either trabeculate or remain in the compact layer (*32*). If actomyosin also plays an earlier role in curvature cell shape acquisition, we would expect to see different presentations of the network between curvatures. Indeed, in zebrafish, where there is a single layer of cardiomyocytes at this stage, visualization of the outer surface of the myocardium has highlighted what is interpreted as “cortical” F-actin in both curvatures (*i.e.* intense F-actin signal outlining each cell) and an additional pool of “cytoplasmic” F-actin running throughout OC cells (*33*). Although visualizations of the F-actin cytoskeleton in chick are somewhat more challenging due to the bilayered myocardium, distinctions between the OC and IC have been resolved, with circumferentially aligned F-actin at cell-cell boundaries in the IC and a less organized network of F-actin in the OC (*34*, *35*). Furthermore, actin dynamics appear to be necessary for the curvature formation process: in both chick and zebrafish, explanted hearts exposed to inhibitors of actin polymerization fail to achieve the stereotypic curved chamber contours (*36–38*). Altogether, these data position actomyosin as a likely regulator of curvature formation, but how the divergence of the actomyosin landscape is regulated and whether the network mediates its effect on tissue shape via active cell shape change remain unknown.

Curvature formation takes place in a heart that is actively beating and pumping blood, suggesting the possible involvement of biomechanical cues in regulating the cellular and subcellular changes that occur in OC and IC cardiomyocytes. It is well known that biomechanical inputs, such as fluid forces stemming from blood flowing through the endocardial lumen, tissue tension arising from the sarcomeric contraction of myocardial cells, and the anchoring of venous and arterial poles to the vascular system, influence several aspects of cardiac development (*12*, *39–44*). For example, altering the dynamics of blood flow in zebrafish can prevent both trabeculation (*19*, *45*, *46*) and valve formation (*47–49*). In addition, zebrafish hearts that lack atrial contractility and thus have reduced blood flow through the ventricle exhibit OC cells with a reduced apical surface area (*25*). This phenotype highlights the importance of extrinsic factors for attaining curvature-linked cell shapes, but it is not yet clear how these forces are translated into the subcellular events that instigate changes to cardiomyocyte morphology.

While extrinsic forces clearly impact curvature formation, factors intrinsic to the myocardium are certainly also involved in regulating the cytoskeleton, changing cell behavior, and ultimately sculpting tissue shape. In considering intrinsic factors that could influence curvature morphogenesis, the TBX family of transcription factors stand out as potentially important contributors. A set of these factors work in concert to pattern the expression of genes associated with the chamber curvatures: TBX5 promotes expression of OC-related genes, whereas TBX2 and TBX3 suppress expression of these genes (*9*, *10*, *50–56*). For example, the combination of these three factors determine the OC-enriched expression of *Nppa* in mice (*51–54*). In zebrafish, expression of *nppa* is already enriched in the future ventricular OC region of the linear heart tube, well before curvatures take shape (*25*). Although loss-of-function analyses indicate that *nppa* itself is not necessary for curvature formation (*57*), its early prepattern signifies that there may be other factors regulated by Tbx factors that could influence the ability of OC or IC cells to change their morphology. This idea is especially intriguing in light of recent work in mouse showing that TBX5 influences epithelial tension and cell morphology in the second heart field (*58*).

In this study, we delve into new aspects of how OC and IC cardiomyocyte morphologies diverge during curvature formation in zebrafish. Specifically, by studying OC and IC cell shapes in three dimensions, we have found that OC cardiomyocytes expand primarily in the planar axis, becoming more squamous as curvatures form, while IC cardiomyocytes extend primarily in the

apicobasal axis, becoming more cuboidal. We show that these cellular changes are preceded by regionalized patterns of subcellular actomyosin organization, and that actomyosin plays a cell-intrinsic role in determining cell shape. Intriguingly, this role appears to be in the induction of planar spread, rather than the role of constriction for which the actomyosin cytoskeleton is so well known. Finally, we show that blood flow through the ventricle and *tbx5a* each promote the curvature-associated divergence of actomyosin organization and cardiomyocyte morphologies, with particularly prominent effects in the OC. From these findings, we propose that several extrinsic and intrinsic factors converge to control the cytoskeletal dynamics that give rise to the characteristic contours of the cardiac chambers.

Results

Curvature formation coincides with the divergence of ventricular OC and IC cardiomyocyte morphologies

To study the cellular and molecular underpinnings of curvature formation, we first needed to develop a working method to standardize the boundaries of the ventricular curvatures. For this purpose, we used a combination of gene expression patterns and measurements of morphological features to guide boundary placement in the embryonic zebrafish heart at 48 hours post-fertilization (hpf) (fig. S1A-C). For gene expression, we relied on *nppa*, which is enriched in the OC of both the ventricle and atrium (*25*, *59*). Generally, the highest-expressing area of the ventricle was deemed to be the OC, and the lowest-expressing area was deemed to be the IC (fig. S1A,C). After examining the *nppa* expression pattern in 12 wild-type hearts at 48 hpf, we used the typical territory of *nppa* expression and its spatial relation to the atrioventricular canal (AVC) and distal end of the outflow tract (OFT) to determine the morphological features of the heart that could serve as boundaries for the curvatures (see Supplementary Materials and Methods for more detail). Once we had drawn these boundaries, we found that the IC region coincided satisfyingly with the expression of *mb* (fig. S1B), a gene previously noted to be enriched in the ventricular IC (*60*). In a wild-type heart at 48 hpf, the OC region typically includes ~50-60 cardiomyocytes, and the IC region typically includes ~25-30 cardiomyocytes. We modified this method slightly to determine the curvature boundaries in wild-type hearts at 36

hpf (fig. S1D; see Supplementary Materials and Methods for more detail), and we used these rules to bound the curvatures in mutant hearts as well (see subsequent figures, including Figs. 5 and 6). Although we think that these boundaries encompass the territories that are important for the study of curvature formation, it is possible that they include some less relevant areas. Nevertheless, this method provides a useful and reproducible strategy for outlining the OC and IC in multiple contexts.

Our previous work shows that certain characteristics of cardiomyocyte shape, such as apical surface area and circularity, are uniform throughout the myocardium at the linear heart tube stage (24 hpf), but eventually diverge in the curvatures by 48 hpf (*25*). Employing our new definitions of the OC and IC, we aimed to understand this divergence with greater temporal detail by looking at a developmental stage midway through curvature formation, in both the planar (X/Y) and apicobasal (Z) axes. At 37 hpf, when curvatures have just started to take shape, we found that OC and IC cardiomyocytes exhibit a modest difference in morphologies (Fig. 1A,B,E-H). OC cells have a slightly but significantly larger apical surface area than IC cells, whereas the circularity of the apical surfaces are comparable (Fig. 1A,E,H). Additionally, cell thickness, as measured by apicobasal length, is similar between OC and IC cells at this stage (Fig. 1B,F). Both OC and IC cells increase in volume between 37 and 48 hpf and extend this new volume in both planar and apicobasal axes (Fig. 1C,D,G). However, OC cells expand along their planar axis to a greater extent than do IC cells (Fig. 1A,C), as observed by a greater increase in apical surface area (Fig. 1E), and they become more elongated, typically along their circumferential axis (Fig. 1H). By contrast, IC cells become taller along their apicobasal axis and remain more circular than OC cells (Fig. 1B,D,F,H). Together, these data suggest that cells in the developing curvatures grow to similar degrees during this time, but they choose to allocate their new volume along different axes: along the planar axis for OC cells and along the apicobasal axis for IC cells. As a consequence, OC cells become more squamous, and IC cells become more cuboidal.

Divergence of cardiomyocyte morphologies is preceded by changes to actomyosin organization

To understand the cellular mechanisms behind the divergence in OC and IC cardiomyocyte shapes, we first wanted to identify when previously reported cytoskeletal

characteristics of the curvatures diverged (*33–35*). Specifically, do the portions of the ventricle that will become the IC and OC exhibit differential actomyosin landscapes as soon as the linear heart tube is formed, or do they diverge sometime during curvature formation? If the latter is true, does this divergence precede the appearance of the observed differences between OC and IC cell shapes? Throughout the process of curvature formation, we found that F-actin primarily resides along the inner surface of the cardiomyocyte membranes. At 28 hpf, when a small bulge of an OC is just becoming evident (fig. S2A), subcellular distribution of F-actin appears fairly uniform around the circumference of the ventricle, including in the presumptive OC and IC (fig. S2A,B). As observed previously (*61*), proximal ventricular cells (those closer to the AVC) exhibit F-actin mostly at their basal membrane (fig. S2A″,B″,B‴), whereas distal ventricular cells (those closer to the OFT) exhibit F-actin distributed around all of the surfaces of their membrane, with particularly strong presence at the apical surface (fig. S2A′,B′,B‴). At 36 hpf, when OC and IC cells have begun to show small morphological differences (Fig. 1A,B,E-H), the F-actin in OC cells remains more enriched at the basal surface, particularly in the proximal ventricle (fig. S2C′, C″,D′,D″). In IC cells, F-actin is distributed more equally around the membrane surfaces, with a substantial amount at the lateral and apical surfaces (fig. S2C′, C″,D‴,D⁗). At 48 hpf, OC and IC cells look fairly similar to each other, with F-actin distributed around all membrane surfaces and particularly intense signal at the lateral membranes (fig. S2E,F). Our observations that OC and IC cells begin with similar F-actin organization but diverge at 36 hpf, only to converge again by 48 hpf, drew our attention to 36 hpf as a stage worthy of more intense study. These findings correspond well with published visualizations of the myocardial surface showing that F-actin organization differs between OC and IC cells at 36 hpf (but not at 24 hpf) (*33*) and that *myosin vb* mutants, which fail to undergo OC cell planar expansion, exhibit aberrant F-actin organization in OC cells at 36 hpf (*62*).

To better understand these qualitative findings, we adopted a more quantitative approach to the examination of the subcellular localization of F-actin and pMyosin in individual cardiomyocytes of the OC and IC (Fig. 2A-E). For every cardiomyocyte analyzed, we quantified signal intensities to reveal what proportion of the total F-actin and pMyosin is localized to its basal, lateral, and apical membranes (Fig. 2B; see Supplementary Materials and Methods for more detail). Using this approach, we found that OC cells have a higher proportion of basal actomyosin than do IC cells (Fig. 2C-E), whereas IC cells have a higher proportion of apical and

lateral actomyosin than do OC cells (Fig. 2C-E). In addition, we wondered whether we could observe disparities between cells in the proximal OC/IC and cells in the distal OC/IC, as we could in fig. S2. Comparing these subsets of cells, we found that proximodistal differences are quite clear in the OC (figs. S3 and S4). In proximal OC cells, F-actin and pMyosin are highly enriched at the basal surface, whereas in the distal OC, cells have a significantly lower proportion of actomyosin at the basal membrane and a higher proportion of actomyosin at the lateral and apical membranes, giving an overall organization more similar to cells of the IC, which do not exhibit striking differences between proximal and distal regions. These data from individual cells (Fig. 2) support what we observed at the tissue level (fig. S2) and highlight a potentially important aspect of cytoskeletal dynamics during a critical period of curvature formation.

Altogether, our observations indicate that, in the linear heart tube, cardiomyocytes in the future OC and IC have similar actomyosin organization, and that the greater disparity lies between the proximal ventricle and the distal ventricle. As chambers begin to form, cells in the OC (particularly those in the proximal region) retain basal enrichment of actomyosin, while cells in the IC accumulate actomyosin at their apical and lateral surfaces. These data suggest that the actomyosin network in cardiomyocytes is differentially regulated depending upon their location within the ventricle. In addition, these data imply potentially distinct roles for actomyosin in the curvatures, given that the precise location of actomyosin within a cell determines its ability to engage drivers of specific cell behaviors.

Modulation of actomyosin dynamics dampens the divergence of OC and IC cardiomyocte morphologies

Given the intriguing regionalized patterns of subcellular actomyosin localization that arise during chamber curvature formation, we wondered whether the actomyosin cytoskeleton plays a role in the divergence of curvature cell shapes. Previous studies in chick and zebrafish have shown that actin polymerization is crucial for chamber curvature formation (*36–38*), but these studies have not delved into the impact of actin polymerization on cardiomyocyte morphology. We treated wild-type embryos from 24-36 hpf or from 36-48 hpf with either Latrunculin B (Lat B) or Blebbistatin (Bleb) to block actin polymerization or non-muscle myosin II (NMII) activity, respectively (fig. S5). In embryos treated with either LatB or Bleb from 24-36

hpf, OC cardiomyocytes exhibited significantly smaller apical surface areas when compared with DMSO-treated controls (fig. S5A,B,D,E,F,H). In contrast to the effects of treatment from 24-36 hpf, Lat B treatment from 36-48 hpf had no effect on planar expansion of OC cells (fig. S5C,D), and, curiously, Bleb treatment from 36-48 hpf resulted in excessive planar expansion (fig. S5G,H). These data highlight 24-36 hpf as a particularly important window for actomyosin activity in promoting OC cell planar expansion. They also hint at a second phase of NMII activity between 36 and 48 hpf, during which Myosin-based contractility might be important for maintaining cell shape.

We next wanted to evaluate whether actomyosin activity is required in cardiomyocytes themselves, or if the effect we observe on cardiomyocyte shape upon LatB or Bleb treatment is due to a required function in another tissue, such as the endocardium. To assess this, we used established transgenic lines to express different versions of the non-muscle myosin light chain 9 gene (*myl9*) driven throughout the myocardium by the cardiomyocyte-specific *myl7* promoter: wild-type *myl9* (*Tg(myl7:WTmyl9-mScarlet)*), a dominant negative version of *myl9* (*Tg(myl7:DNmyl9-eGFP)*), or a constitutively active version of *myl9* (*Tg(myl7:CAmyl9-eGFP)*) (*32*). When assessing cardiomyocyte morphologies at 48 hpf, we found that expression of *WT-myl9* resulted in cell morphologies fairly reminiscent of those in wild-type embryos (Figs. 1C-F,H and 3A,B,G-I). By contrast, expression of *DN-myl9* resulted in OC cardiomyocytes with decreased apical surface area and increased apicobasal length when compared with OC cells expressing *WT-myl9* (Fig. 3C,D,G,H). Together, these changes resulted in a more cuboidal phenotype. Additionally, IC cells expressing *DN-myl9* exhibited a slightly (but significantly) decreased apical surface area and equivalent apicobasal length when compared with those expressing *WT-myl9* (Fig. 3C,D,G,H). Expression of *CA-myl9* resulted in OC cells with a slightly (but significantly) decreased apical surface area and increased apicobasal length when compared with those expressing *WT-myl9*, whereas IC cells expressing *CA-myl9* exhibited a similar apical surface area and slightly (but significantly) decreased apicobasal length when compared with those expressing *WT-myl9* (Fig. 3E,F,G,H). Interestingly, both OC and IC cells expressing *CA-myl9* were more elongated than those expressing *WT-myl9* (Fig. 3I). Altogether, these data suggest that actomyosin dynamics are indeed important within the myocardium to support the divergence of OC and IC cell morphologies, and that modulating NMII activity produces OC and IC cells with ultimately similar shapes.

To better understand the effect of these transgenes on cardiomyocyte shape, we wondered whether the changes in NMII activity that led to cell shape alterations also had a parallel effect on the F-actin network. We were intrigued to find that expression of *DN-myl9* or *CA-myl9* reduced the overall amount of F-actin in the ventricle at 36 hpf (fig. S6). We further found that subcellular localization of F-actin was disrupted in both the *DN-myl9* and *CA-myl9* contexts, and in cardiomyocytes of both curvatures (fig. S7). Of particular interest, we found a shift in F-actin enrichment from the basal membrane to the apical and lateral membranes in *DN-myl9*-expressing (fig. S7B,G) and *CA-myl9*-expressing (fig. S7C,G) OC cells. This shift prompted us to quantify the ratio of the amount of F-actin at the basal membrane to the amount of F-actin at the apical and lateral membranes (basal / (apical + lateral)). This ratio revealed a striking shift away from the basal enrichment normally seen in *WT-myl9*-expressing OC cells (fig. S7H). From other contexts, we know that Myosin can support F-actin bundles by crosslinking (*63–65*), can induce disassembly of stress fibers (*66–68*), and can organize F-actin at specific locations within the cell (*69–71*). Therefore, although we do not yet understand the exact reason that expression of *DN-my9* or *CA-myl9* disrupts the F-actin network so severely, it is perhaps not surprising that it does so.

NMII function plays a cell-intrinsic role in promoting divergence of OC and IC cardiomyocyte morphologies

Having seen that cardiomyocytes fail to attain expected shapes when either a dominant negative or constitutively active form of NMII is expressed throughout the myocardium (Fig. 3), we were curious about whether actomyosin plays a cell-intrinsic role in promoting OC and IC cell shape divergence, or, rather, if NMII-driven tissue-level tensions are responsible for the acquisition of cell morphologies. We therefore performed blastomere transplantation to create genetically mosaic animals (Fig. 4A). In these experiments, we analyzed hearts that contained donor-derived cardiomyocytes expressing *CA-myl9* or *DN-myl9* surrounded by host-derived wild-type cardiomyocytes (Fig. 4B-M; see Materials and Methods regarding how specific cardiomyocytes were chosen for analysis). In comparison with their wild-type host-derived neighbors, *CA-myl9*-expressing OC cells had a dramatically decreased apical surface area and increased apicobasal length, resulting a strikingly more cuboidal phenotype (Fig. 4B,C,E,F). In addition, *CA-myl9*-expressing donor-derived OC cells were significantly more circular than their

wild-type neighbors (Fig. 4B,C,G). In the IC, *CA-myl9*-expressing donor-derived cells were also more cuboidal than their host-derived wild-type neighbors, but the magnitude of this effect was less than in the OC (Fig. 4B,D-F). This OC phenotype is particularly interesting, given its contrast to the effect of uniform expression of *CA-myl9* throughout the myocardium (Fig. 3E-I), in which cardiomyocytes were only slightly more cuboidal and were in fact more elongated than *WT-myl9*-expressing cells. This disparity highlights the importance of tissue-scale tension and how individual cell shape can be influenced depending on whether neighboring cells exhibit normal or increased tensions.

In the dominant negative situation, we found that *DN-myl9*-expressing OC cardiomyocytes had a smaller apical surface area when compared with *WT-myl9*-expressing cells (Fig. 4H,I,K), but that apicobasal length was unchanged (Fig. 4H,I,L). In the IC, we found that *DN-myl9*-expressing donor-derived cells were very similar to their host-derived neighbors (Fig. 4H,J-M). This OC cell phenotype is fairly similar to the effect of uniform expression of *DN-myl9* throughout the myocardium (Fig. 3C,D,G-I). These data indicate that NMII plays a cell-intrinsic role in promoting the planar expansion of OC cells and that this role is not altered by the degree of tension in neighboring cells. Taken together, our analysis of cardiomyocytes expressing *myl9* transgenes emphasizes that actomyosin activity supports the divergence of OC and IC cell shapes by promoting the squamous identity of OC cells in a cell-intrinsic manner, perhaps by facilitating active expansion in the planar axis, as has been hypothesized (*37*). In contrast, IC cells appear to be affected only when actomyosin contractility is intensified throughout the process of curvature formation, as is the case with *CA-myl9* expression.

Divergence of OC and IC actomyosin organization and cardiomyocyte morphology is sensitive to cardiac function

Our results thus far had highlighted actomyosin organization and function as drivers of cell shape change during curvature formation, and we next wanted to know what types of upstream regulators might control these subcellular features. We were particularly curious to evaluate how blood flow might affect actomyosin localization and cardiomyocyte morphology, as our previous work has shown that *myosin heavy chain 6* (*myh6*) mutants (*72*), which lack an atrium-specific myosin heavy chain and therefore lack atrial contractility, have reduced blood flow through the ventricle as well as reduced apical surface area of OC cardiomyocytes (*25*).

Consistent with previous findings, we found that OC cells of *myh6* mutants fail to extend along the planar axis (Fig. 5A,C,E). In addition, we observed that OC cells also extend inappropriately along the apicobasal axis (Fig. 5B,D,F). Taken together, these data indicate that *myh6* OC cells acquire a more cuboidal phenotype than their wild-type counterparts. In contrast to the OC results, we found that the apical surface area and apicobasal length of *myh6* IC cells are indistinguishable from those of wild-type IC cells (Fig. 5A-F); however, both OC and IC cells exhibit a modest but significant decrease in volume in *myh6* mutants (Fig. 5G).

Given the effect of reduced blood flow on OC cell morphology, we next asked if this phenotype is coupled with a disordered actomyosin cytoskeleton. We found that the overall levels of F-actin in the ventricular myocardium in *myh6* mutants at 36 hpf are reduced relative to wild-type (similar to our observations in *DN-myl9* and *CA-myl9* transgenic hearts (fig. S6)), whereas the levels of pMyosin are comparable to wild-type (fig. S8A-D). In addition to an overall deficit in F-actin, we found mislocalization of subcellular actomyosin in *myh6* mutant OC cells (Fig. 5I-L,O,P): both F-actin and pMyosin shift away from the basal surface and to the lateral and apical surfaces in the proximal OC and distal OC, with a particularly striking shift in the proximal OC (Fig. 5K,L,O,P; fig. S8E). In contrast to this OC cell phenotype, both F-actin and pMyosin organization in *myh6* mutant IC cells are comparable to wild-type (Fig. 5M-P; fig. S8E). Taken together, these data highlight a previously unappreciated role for extrinsic factors such as blood flow in ensuring the regionalization of cytoskeletal landscapes and, subsequently, the planar expansion of OC cells.

Cell-autonomous function of *tbx5a* contributes to the divergence of OC and IC actomyosin organization and cardiomyocyte morphology

Alongside considering the extrinsic factors that influence curvature formation, we also wondered what types of intrinsic factors, operating within individual cells, could impact the divergence of cardiomyocyte cell shapes and actomyosin organization. We were particularly curious about the influence of the T-box transcription factor gene *tbx5a*. In addition to the known role for *Tbx5* in promoting OC transcriptional programs (*50*, *51*, *55*), zebrafish homozygous for mutant alleles of *tbx5a* exhibit a dramatically dysmorphic heart by 48 hpf (*9*, *73*). As reported previously (*73*), the outward bulge of the *tbx5a* mutant OC is vastly reduced and the *tbx5a* mutant IC exhibits less of a kink when compared with a wild-type heart (Fig. 6A,C). We

therefore investigated whether *tbx5a* mutant cardiomyocytes underwent the stereotypical divergence in shape associated with the ventricular curvatures. At the cellular scale, and similar to the phenotypes seen in *DN-myl9*-expressing hearts (Fig. 3A-D,G,H) and in *myh6* mutants (Fig. 5A-F), OC cells in *tbx5a* mutants fail to expand in the planar axis and undergo aberrant apicobasal expansion (Fig. 6A-F). This combination results in *tbx5a* mutant OC cells with a more cuboidal phenotype than wild-type OC cells. Interestingly, even though at the tissue level *tbx5a* mutant ICs fail to form the stereotypic kink (Fig. 6C), IC cell shapes in *tbx5a* mutants appear relatively normal with just a slight trend toward reduction in apicobasal length (Fig. 6A-F). In contrast to *myh6* mutants (Fig. 5G,H), *tbx5a* OC and IC cells exhibit volumes and circularity similar to that of wild-type cells (Fig. 6G,H).

We next wondered whether the effect of *tbx5a* loss-of-function on OC cardiomyocyte morphology was preceded by a dysregulation of the actomyosin cytoskeleton. Similar to the *DN-myl9* (fig. S6A,B,D) and *myh6* (fig. S8A-D) phenotypes, the overall levels of F-actin in the *tbx5a* mutant ventricular myocardium are reduced at 36 hpf, whereas levels of pMyosin are comparable to wild-type (fig. S9A-D). In addition to an overall deficit in F-actin, we found mislocalization of subcellular F-actin and pMyosin, and this was particularly prominent in the proximal OC (Fig. 6I-P). In the *tbx5a* mutant proximal OC, F-actin and pMyosin enrichment shift away from the basal surface and accumulate more at the lateral and apical surfaces (Fig. 6O,P; fig. S9E). In distal OC and in IC cells, F-actin is also shifted laterally and apically (albeit to a lesser extent than in the proximal OC), but the ratio of basal to apical/lateral pMyosin is comparable to wild-type (Fig. 6O,P; fig. S9E). Intriguingly, in contrast to the *myh6* scenario where the effect on pMyosin localization is very similar to the effect on F-actin localization (Fig. 5O,P; fig. S8E), the F-actin phenotype observed in *tbx5a* mutants is more severe than the pMyosin phenotype (Fig. 6O,P; fig. S9E). Overall, these data suggest that Tbx5a-regulated pathways are particularly important for the enrichment of F-actin at the basal surface of OC cells.

Given the actomyosin and cell morphology phenotypes in flow-deficient *myh6* mutants (Fig. 5) and the reduced heart rate in *tbx5a* mutants (*73*), we wondered whether the aberrant effects on F-actin localization in *tbx5a* mutants reflect indirect consequences of altered blood flow or an intrinsic loss of *tbx5a* function. To address this, we took a mosaic approach in which we transplanted wild-type blastomeres into *tbx5a* mutant host embryos and *tbx5a* mutant blastomeres into wild-type host embryos at ~3 hpf, as well as performing wild-type into wild-

type and mutant into mutant controls (Fig. 7A-D). We fixed host embryos at 36 hpf and assessed amounts of F-actin at basal, lateral, and apical membranes (Fig. 7E-P: fig. S10). In a *tbx5a* into wild-type scenario, we found that the F-actin organization in *tbx5a* mutant donor-derived proximal OC cells largely resembled that of their wild-type neighbors (Fig. 7K,M; fig. S10C), indicating that something about the wild-type environment can rescue this aspect of the *tbx5a* mutant phenotype. In light of this result, we were particularly intrigued by the wild-type into *tbx5a* scenario. Here, we found that wild-type donor-derived cells in a *tbx5a* mutant proximal OC contained a significantly higher proportion of basal F-actin compared with apical and lateral F-actin, when compared with their *tbx5a* mutant neighbors (Fig. 7H,J; fig. S10B). This suggests an ability of wild-type cells to organize their F-actin network regardless of the *tbx5a* status of surrounding cells. Together, these data indicate that there is at least a partially cell-autonomous role for *tbx5a* in establishing the divergent actomyosin organization observed in the developing curvatures, but that there are also likely to be non-autonomous ways that *tbx5a* influences actomyosin organization.

We next wanted to know whether *tbx5a* also plays a cell-autonomous role in promoting the divergence of OC and IC cardiomyocyte morphologies. We used the same experimental scheme as in Fig. 7, but we fixed host embryos at 48 hpf and assessed cardiomyocyte shapes (fig. S11). Interestingly, consistent with our analysis of actomyosin localization in wild-type into *tbx5a* mosaic hearts (Fig. 7H,J), wild-type donor-derived OC cells extended in the planar axis significantly more than their *tbx5a* mutant host-derived neighbors, allowing them to assume a more squamous identity (fig. S11I,K,L). Also like our mosaic analysis of actomyosin localization (Fig. 7K,M), *tbx5a* mutant donor-derived cells that reside in a wild-type OC largely exhibit morphology similar to their wild-type neighbors (fig. S11M,O,P). Finally, donor-derived IC cells in both wild-type into mutant and mutant into wild-type scenarios achieve morphologies similar to their host-derived neighbors (fig. S11J-L,N-P). Taking our transplantation experiments together, it appears that the environment of a wild-type heart is able to largely override the absence of *tbx5a* function in donor-derived mutant cardiomyocytes, but, conversely, wild-type cells are capable of achieving stereotypical OC traits even in a *tbx5a* mutant background. This suggests that the ventricular phenotypes we see in *tbx5a* mutants are not solely due to defects in blood flow and that there is some cell-autonomous aspect to *tbx5a* function during curvature formation.

An unexpected finding from our mosaic studies was that, in some cases, donor-derived cells sent basal projections underneath their host-derived neighbors (fig. S12). We observed such projections in all four of our transplant scenarios; these projections were typically rather short and slim and were usually restricted to the junctions between neighboring cells (fig. S12C,D,I). However, in the wild-type into *tbx5a* mutant transplant scenario, it was not uncommon for wild-type donor-derived OC cells to send long, broad projections underneath the cell body of a neighboring *tbx5a* mutant host-derived cell (fig. S12E-I). This could be a reflection of the comparatively robust ability of wild-type cells to expand their basal domain, a relatively reduced cell-extracellular matrix (ECM) connection in *tbx5a* mutant tissue, or both. This idea is further supported by the observation that, in the same wild-type into *tbx5a* mutant scenario, donor-derived OC cells that did not contact any other donor-derived OC cells (*i.e.* those in single-cell clones) had, on average, a higher apical surface area than donor-derived OC cells that contacted other donor-derived cells (fig. S13A). Further morphological assessment of these single-cell clones showed that all of them sent out basal projections: 3 of the 7 clones sent thin basal projections that extended between the junctions of neighboring host cells (fig. S13B,C), and the remaining four sent larger basal projections underneath neighboring host-derived cell(s) (fig. S13D,E). We propose that this ability to send basal projections is a mechanism that normally drives planar expansion of OC cells, and that this activity is increased when neighboring cells maintain a looser attachment to the underlying ECM.

Discussion

Our analysis of the cellular and subcellular dynamics of individual cardiomyocytes within the developing ventricle has provided a series of new insights into the mechanisms that drive the morphological divergence of OC and IC cells and their contributions to chamber curvature formation. Although cardiomyocytes in both curvatures increase in volume during curvature emergence, cells in the OC expand preferentially in the planar axis, whereas cells in the IC expand preferentially in the apicobasal axis. These contrasting behaviors are preceded by a divergence in subcellular actomyosin localization between the curvatures. Further, modulation of actomyosin activity affects the ability of OC cells to attain the expected squamous shape, indicating that the actomyosin network plays an important role in promoting squamous instead of

cuboidal cardiomyocyte morphologies. Finally, the regionalized distinctions between the actomyosin landscapes and, subsequently, cell morphologies in the curvatures are influenced by both extrinsic factors, such as blood flow through the ventricle, and intrinsic factors, like the transcription factor gene *tbx5a*.

Taken together, our data suggest a novel model in which regional regulation of the actomyosin cytoskeleton mediates the planar expansion of OC cells, ultimately causing a divergence in OC and IC cell morphologies during the critical period of curvature formation (Fig. 8). Prior to the onset of curvature formation, the largest distinctions in actomyosin organization within the ventricle are primarily proximal versus distal (Fig. S2), in agreement with previous reports (*61*). As development proceeds, however, differences begin to emerge between the subcellular landscapes of OC and IC cells. Specifically, cells throughout the proximodistal length of the IC acquire more apical actomyosin, whereas cells especially in the proximal OC maintain strong basal localization of actomyosin (Fig. 2 and fig. S3). We propose that this basal enrichment of actomyosin promotes planar expansion, perhaps by engaging the focal adhesion machinery. The coincident lack of actomyosin at the apical surface of proximal OC cells may allow for low localized tension, ensuring that the apical surface can passively expand along with the actively expanding basal surface. In the IC, we speculate that the redistribution of actomyosin away from the basal surface reduces certain associations with the ECM and therefore reduces outward pushing forces; simultaneously, more actomyosin at the apical surface could play a more active and stereotypically contractile role in maintaining a compact apical surface area. Thus, we envision that the actomyosin landscapes in each curvature support OC cells in expanding outward along the planar axis and IC cells in remaining more constricted.

This model of contrasting OC and IC cell behaviors is also supported by aspects of our mosaic analyses. For example, we found that wild-type cells in the midst of a *tbx5a* mutant OC often send large, broad projections underneath neighboring mutant cells, whereas wild-type cells in a wild-type OC send much smaller projections that are usually restricted to cell junctions (figs. S12 and S13). This suggests that wild-type OC cells have a mechanism for sending projections, and that *tbx5a* mutant OC cells (which, at the earlier stage of 36 hpf, have a reduced pool of basal actomyosin (Fig. 6 and fig. S9)) may have a weakened connection to the underlying ECM. In addition, we found that cells expressing *DN-myl9* (which also exhibit dysregulated

actomyosin localization at 36 hpf (fig. S7)) do not undergo proper planar expansion when surrounded by either wild-type cells (Fig. 4) or other *DN-myl9*-expressing cells (Fig. 3). These data suggest that cells with reduced actomyosin activity or disrupted F-actin organization are not capable of the outward pushing behavior that we propose enables planar expansion in the OC. Intriguingly, recent work has identified actin-based protrusions that drive the elongation of zebrafish atrial cardiomyocytes as the atrial wall thickens after 72 hpf (*74*), and we are keen for our future work to explore whether similar protrusions promote planar expansion in the ventricular OC.

Although our model of outward pushing contrasts with the frequent demonstration that actomyosin constricts cell boundaries during morphogenesis, the idea that a growing actin cytoskeleton could force cardiomyocyte membranes outward during curvature formation was originally put forth by Latacha and colleagues nearly two decades ago (*37*). Additionally, we know that this effect of the actin cytoskeleton is necessary in other contexts. For example, in the leading edge of migrating cells, actin branching, polymerization, and depolymerization pushes the membrane outward, specifically in the direction of movement (*75–77*). These pushing forces are also observed in epithelial contexts: in the *Xenopus* epidermis, cell-autonomous actin dynamics at the apical surface drive outward pushing and thus apical emergence of multiciliated cells (*78*, *79*), and, in *Drosophila* follicle cells, actomyosin and its association with the ECM promotes expansion of the basal surface, resulting in cell flattening and tissue elongation (*80*, *81*). It would be valuable for future studies to explore potential mechanistic similarities between these contexts and the planar spread of OC cardiomyocytes.

Our data clearly indicate that both extrinsic and intrinsic factors contribute to the regulation of the divergent cytoskeletal landscapes observed in the ventricular curvatures. For the former, we demonstrated that mutants with reduced blood flow through the ventricle not only fail to acquire the expected OC cell morphologies, as previously reported (*25*), they also exhibit earlier defects in the OC actomyosin network (Fig. 5). Specifically, in *myh6* mutants, F-actin levels are dramatically reduced throughout the ventricular myocardium (fig. S8) and both F-actin and pMyosin are shifted away from the basal membrane to the lateral and apical membranes in OC cells (Fig. 5). For the latter, we found that *tbx5a* mutants, already appreciated for their underformed curvatures (*9*, *73*), also exhibit reduced F-actin levels (fig. S9), shifted F-actin away from the basal membrane in OC cells (Fig. 6), and defects in the planar expansion of OC cells

(Fig. 6). It is interesting to note that reduced blood flow and loss of *tbx5a* function both primarily impacted cells in the OC; although both curvatures are exposed to blood flow and *tbx5a* is expressed throughout the ventricular myocardium (*73*), these factors do not influence the cytoskeleton in IC cells to the same extent that they do in OC cells. This intimates the existence of yet unidentified curvature-specific factors that could help translate extrinsic and intrinsic influences into cytoskeletal changes. More broadly, it will be valuable for future work to identify and investigate a roster of actomyosin modifiers whose expression or activity may be regulated, even indirectly, by blood flow or by *tbx5a*. One interesting candidate is *adducin3a* (*add3a*), which is regulated by a heartbeat-dependent microRNA, *miR-143*, and encodes an F-actin capping protein that stabilizes actin polymers (*33*, *82*, *83*). Overexpression of *add3a* has been shown to prevent planar expansion of OC cells, likely due to the hyperstabilization of the actin cytoskeleton (*33*), suggesting that regionalized regulation of Add3a activity could contribute to the normal acquisition of OC cell morphology. In addition, it will be interesting to investigate whether any TBX5 targets that may mediate myosin phosphorylation in the mouse second heart field epithelium (*58*) also function downstream of Tbx5a to modify actomyosin in the OC.

Although actin dynamics have long been implied as a driver of chamber curvature formation, the role of NMII has been debated, with some studies dismissing its role and others supporting it. For example, chick embryos or explanted hearts treated with inhibitors of NMII just after the initiation of curvature formation go on to form relatively normal curvatures (*84*). By contrast, explanted zebrafish heart tubes treated with Blebbistatin fail to form chamber curvatures (*38*). Of course, these disparate findings could simply signify differences between species. However, our studies offer an alternative explanation in which there are at least two distinct phases of the influence of actomyosin on the regulation of cardiomyocyte shape. Our treatments with Blebbistatin or Latrunculin B (fig. S5) imply that, early in curvature formation (~24-36 hpf), both actin polymerization and NMII activity are required to allow the subsequent planar expansion of OC cells. In contrast, later in curvature formation (~36-48 hpf), actin polymerization does not seem to impact OC cell planar expansion, and NMII even plays the opposing role of restricting planar spread, presumably due to its canonical contractile properties. These findings, together with the impact of DN-Myl9 and CA-Myl9 activity on both total F-actin (fig. S6) and subcellular localization (fig. S7), support a model wherein the early F-actin dynamics that are crucial for subsequent OC cell shape change may be regulated by NMII.

Indeed, the influence of NMII on F-actin dynamics is a commonly reported phenomenon (*63–71*), and we therefore recommend special attention to the timing of any such actomyosin manipulations in studies of curvature formation. The perduring activity of DN-Myl9 and CA-Myl9 throughout curvature formation in our experiments may cloud our interpretations, as their aberrant activity during later curvature formation could suppress the effects of their earlier activity (and *vice versa*). In future studies, having both spatial and temporal control over actomyosin cytoskeleton modification will help to test these ideas more directly.

Cardiac looping involves the coordination of several morphogenetic events in both the ventricle and the atrium, as well as in structures like the OFT and AVC. However, the degree of interdependence of events in these different domains remains unclear. *Ex vivo* studies in zebrafish suggest that accretion of second heart field cells to the outflow and inflow tract regions are not required for the repositioning of chambers, torsion, or formation of the curvatures (*9*, *38*), implying that these processes exhibit some level of independence. In contrast, modulation of Bmp signaling in the AVC and IC leads to reduced chamber displacement, including a fairly unkinked IC; in this context, the OC still forms, but with less convexity when compared with wild-type (*85*), highlighting a link between AVC and IC morphogenesis. Our studies show that it is primarily the OC that is influenced by blood flow and *tbx5a* (Figs. 5 and 6) and that the cell-autonomous effects of *tbx5a* and of *DN-myl9* expression are only observed in the OC (fig. S11 and Fig. 4), suggesting that the pathways studied here are mostly relevant to OC development. Taking these data together, we speculate that the shape of the IC is largely coupled to morphogenesis of the AVC, whereas OC dynamics and shape are driven by the cell-intrinsic, actomyosin-based mechanisms presented here. However, we cannot rule out the possibility of interplay between OC and IC morphogenesis or the potential interaction of OC formation with other elements of looping, such as torsion and chamber displacement. We posit that future use of methods that alter gene function in larger but distinct territories – such as throughout the entire OC – will help to answer these questions.

Altogether, our work supports the notions that intrinsic regulators and extrinsic inputs converge to control the actomyosin cytoskeleton in the OC, that these events are crucial for changes to cell morphology, and that this ultimately leads to the proper sculpting of the ventricle. These findings offer a mechanistic framework both for the specific circumstance of cardiac chamber emergence and for tissue curvature formation in general. In addition, they provide a

foundation for further articulation of the pathways that create the distinctions between the OC and IC, which could ultimately shed light on the origins of certain types of congenital defects in chamber morphology and could also enhance efforts to engineer ventricular tissue *in vitro*.

Materials and Methods

Zebrafish

The following transgenic lines were used in this study: *Tg(myl7:WT-myl9-mScarlet)*^{bns524Tg} (*32*), *Tg(myl7:DN-myl9-eGFP)*^{bns333Tg} (*32*), *Tg(myl7:CA-myl9-eGFP)*^{bns332Tg} (*32*), *Tg(myl7:eGFP-Hsa.HRAS)*^{s883Tg} (*86*), and *Tg(myl7:mKate-CAAX)*^{sd11Tg} (*87*). We also used lines carrying the *tbx5a*^{m21} (*73*) and *myh6*^{m58} (*72*) mutations. Heterozygous carriers of mutations were identified by PCR amplification and subsequent restriction enzyme digest, as previously described for *tbx5a*^{m21} (*30*) and *myh6*^{m58} (*87*). Homozygous mutant embryos were identified by previously characterized morphological phenotypes (*72*, *73*). All work presented here followed protocols approved by the Institutional Animal Care and Use Committee at the University of California, San Diego.

Pharmacological treatments

Embryos were dechorionated and placed in 6-well culture dishes and exposed to either 1.25% DMSO, 1.25% DMSO + 100 ng/mL Latrunculin B (Millipore Sigma, L5228), or 1.25% DMSO + 30 µM Blebbistatin (Millipore Sigma, B0560) in E3 medium. DMSO controls were kept in solution between 24-48 hpf. Latrunculin B and Blebbistatin treated embryos were either kept in drug-containing media between 24-36 hpf and switched to 1.25% DMSO between 36-48 hpf, or *vice versa*. At 48 hpf, all embryos were fixed and processed as described below.

Immunofluorescence and phalloidin staining

Embryos were dechorionated, fixed in 1% methanol-free formaldehyde (ThermoFisher Scientific, 28908) for 1 hour and 10 minutes with gentle rocking, and then rinsed three times in PBT (1X PBS containing 0.1% Tween 20 (Sigma-Aldrich, P9416)). Embryos were rocked rapidly in a 0.2% saponin solution (Sigma-Aldrich, S4521) in PBT containing 0.5% Triton X-

100 (G-Biosciences, 786513) until yolks were dissolved. This took 20-35 minutes and was monitored under a dissecting microscope. Embryos were rinsed three times in PBT, placed in 4% formaldehyde, and incubated at 4°C overnight. On the following day, to improve antibody signal-to-noise ratio, embryos were rinsed three times in PBT, placed in prechilled 100% acetone, and incubated at -20°C for 8 minutes. Acetone was replaced with PBT + 0.5% Triton X-100 for one hour at room temperature. To ensure reagent access to the heart, forceps were used to open the pericardial cavity. Embryos were then blocked with 2 mg/ml bovine serum albumin (Sigma-Aldrich, A9647) and 10% goat serum in PBT for at least one hour at room temperature, then incubated with primary antibody in block overnight at 4°C. Embryos were then washed extensively with PBT, blocked as described for primary antibody incubation, and incubated with the secondary antibodies in blocking solution overnight at 4°C. Embryos were then washed extensively with PBT.

The following primary antibodies were used at the specified dilutions: mouse anti-Alcama (Developmental Studies Hybridoma Bank, Zn-8 supernatant, 1:50); rabbit anti-Cdh2 (GeneTex, GTX125885, 1:200); rabbit anti-phospho-Myosin (Abcam, ab2480, 1:100); rabbit (Life Technologies, A11122, 1:500) or chicken (Life Technologies, A10262, 1:1000) anti-GFP; rabbit anti-dsRed (also detects mScarlet; Clontech, 632496, 1:1000); rabbit anti-TagRFP (also detects mKate; Evrogen, AB233, 1:500); mouse anti-myosin heavy chain (Developmental Studies Hybridoma Bank, MF20 supernatant, 1:50); and mouse anti-Myh6 (Developmental Studies Hybridoma Bank, S46 supernatant, 1:50).

All secondary antibodies were produced in goat by ThermoFisher Scientific and used at a dilution of 1:300. Secondary antibodies used were: anti-mouse-AlexaFluor 488 (A11001); anti-mouse-AlexaFluor 568 (A11031); anti-mouse-AlexaFluor 647 (A21236); anti-rabbit AlexaFluor 488 (A11008); anti-rabbit AlexaFluor 568 (A11011); anti-rabbit AlexaFluor 647 (A21245); and anti-chicken AlexaFluor 488 (A11039). In some cases, Phalloidin-AlexaFluor 488 or Rhodamine-Phalloidin (Life Technologies, A12379 or R415; each reconstituted to 200U/mL in MeOH) was added to the secondary antibody solution at a dilution of 1:30.

Fluorescent *in situ* hybridization

Fluorescent *in situ* hybridization was performed as previously described (*88*), but embryos were fixed and deyolked as for immunofluorescence before MeOH dehydration and

were incubated with Proteinase K (50 µg/mL) in PBT for 2 minutes at room temperature prior to hybridization with probe. Probe for *nppa* (ZDB-GENE-030131-95) was produced as previously described (*72*). Probe for *mb* (ZDB-GENE-040426-1430) was produced by PCR amplification of 48 hpf embryonic cDNA followed by T7 *in vitro* transcription. The forward primer used was 5′-GGACAAACACCGCGACAGAC-3′ and the reverse primer used was: 5′-TAATACGACTCACTATAGGGCCTGAGACCCTAACGAACCATTAT-3′; underlined portion is the T7 binding site.

Transplantation

Blastomere transplantation was performed similarly to a previous description (*25*). Briefly, donor embryos were injected with 5% lysine-fixable rhodamine dextran (ThermoFisher Scientific, D1817) in 0.2M KCl at the one-cell stage. Approximately 10-30 blastomeres were taken from dechorionated 3-4 hpf donor embryos and placed into the margin of similarly staged host embryos. Host embryos were raised in E3 medium containing penicillin-streptomycin (Millipore Sigma, P4458; diluted 1:50), in agarose-coated wells. Host embryos were allowed to develop until 36 or 48 hpf when they were screened for the presence of donor-derived cells in the myocardium, which could be identified by fluorescence under a Zeiss Axiozoom microscope. Hosts containing donor-derived cardiomyocytes were fixed and processed for immunostaining as described above. In order to be included for analysis, cardiomyocytes needed to meet specific criteria. For donor-derived cells, we analyzed any cell with at least half of its body within the OC or IC boundary. For host-derived cells, we analyzed any cell (1) in direct contact with a donor-derived cell or one cell-distance from a donor-derived cell and (2) with at least half of its body within the OC or IC boundary.

For *Tg(myl7:CA-myl9-eGFP)* and *Tg(myl7:DN-myl9-eGFP)* transplants, transgenic animals were crossed to wild-type animals, and the resulting embryos served as donors; wild-type embryos served as hosts. For the *tbx5a* transplantation experiments, animals heterozygous for the *tbx5a* mutation were crossed to obtain both donor and host embryos. After transplantations were complete, donor embryos were genotyped by PCR and restriction enzyme digest for the *tbx5a* mutation, as described above. Genotypes of host embryos were determined based on the presence or absence of pectoral fin buds at 36 hpf or pectoral fins at 48 hpf (*73*).

Image acquisition and analysis

After all immunostaining and fluorescent *in situ* hybridization procedures, hearts were dissected from embryos under a Zeiss AxioZoom microscope. To keep organ morphology as intact as possible, hearts were simply mounted in a droplet of PBT on a cover slip and immediately imaged using a Leica SP8 laser-scanning confocal microscope and a 25X water-immersion objective. In all experiments where signal intensity was measured, laser settings were kept consistent between samples. Z-stacks were captured with a slice thickness of 0.3 µm.

All image files captured by the Leica SP8 confocal were rendered as 3D reconstructions in Imaris (Bitplane). Often, secondary analysis was completed in FIJI (ImageJ). For details of the protocols used to define the ventricular OC and IC and to quantify cardiomyocyte morphometrics, subcellular actomyosin localization, and total actomyosin in the ventricular myocardium, please refer to the Supplementary Materials and Methods.

Statistical analysis

Statistics were performed in R (*89*) and RStudio (*90*) (refer to Supplementary Materials and Methods for more detail). For all comparisons, statistical significance was determined by the Wilcoxon test, which does not assume normal data distribution. Statistically significant p-values are indicated in graphs by asterisks as follows: * denotes $p<0.05$; ** denotes $p<0.01$; *** denotes $p<0.001$. All experiments were performed at least two independent times, and the exact number of embryos and/or cells examined for each experiment is reported in the corresponding figure legend.

Acknowledgments

We thank members of the Yelon laboratory for valuable discussions, A. Negrete and M. Ayan for help with genotyping, and A. Yarbrough and the UCSD Animal Care Program for zebrafish care.

Funding

American Heart Association grant 23TPA1072669 (DY)

Saving tiny Hearts Society (DY)

National Institutes of Health fellowship F32 HL147435 (DML)

American Heart Association fellowship 20POST35110077 (DML)

Max Planck Society (DYRS)

EMBO fellowship LTF1569 (RP)

Alexander von Humboldt Foundation fellowship (RP)

Cardio-Pulmonary Institute grant EXC 2026 project ID 390649896 (RP)

Author contributions

Conceptualization: DML, DY

Data curation: DML, DY

Formal analysis: DML, GBA, DY

Methodology: DML, GBA, DY

Investigation: DML, GBA, DY

Resources: DML, RP, DYRS

Visualization: DML, DY

Validation: DML, DY

Supervision: DYRS, DY

Writing—original draft: DML

Writing—review & editing: DML, GBA, RP, DYRS, DY

Competing interests

Authors declare that they have no competing interests.

Data and materials availability

All data are available in the main text or the supplementary materials. Materials, Excel spreadsheets, and raw images are available upon request to the corresponding author.

References

1. B. Schamberger, R. Ziege, K. Anselme, M. Ben Amar, M. Bykowski, A. P. G. Castro, A. Cipitria, R. A. Coles, R. Dimova, M. Eder, S. Ehrig, L. M. Escudero, M. E. Evans, P. R. Fernandes, P. Fratzl, L. Geris, N. Gierlinger, E. Hannezo, A. Iglič, J. J. K. Kirkensgaard, P. Kollmannsberger, Ł. Kowalewska, N. A. Kurniawan, I. Papantoniou, L. Pieuchot, T. H. V. Pires, L. D. Renner, A. O. Sageman-Furnas, G. E. Schröder-Turk, A. Sengupta, V. R. Sharma, A. Tagua, C. Tomba, X. Trepat, S. L. Waters, E. F. Yeo, A. Roschger, C. M. Bidan, J. W. C. Dunlop, Curvature in Biological Systems: Its Quantification, Emergence, and Implications across the Scales. *Advanced Materials* **35**, 2206110 (2023).
2. T. Savin, N. A. Kurpios, A. E. Shyer, P. Florescu, H. Liang, L. Mahadevan, C. J. Tabin, On the growth and form of the gut. *Nature* **476**, 57–62 (2011).
3. M. Leptin, B. Grunewald, Cell shape changes during gastrulation in *Drosophila*. *Development* **110**, 73–84 (1990).
4. D. Sweeton, S. Parks, M. Costa, E. Wieschaus, Gastrulation in *Drosophila:* the formation of the ventral furrow and posterior midgut invaginations. *Development* **112**, 775–789 (1991).
5. A. C. Martin, M. Gelbart, R. Fernandez-Gonzalez, M. Kaschube, E. F. Wieschaus, Integration of contractile forces during tissue invagination. *Journal of Cell Biology* **188**, 735–749 (2010).
6. J. Männer, Cardiac looping in the chick embryo: A morphological review with special reference to terminological and biomechanical aspects of the looping process. *Anat. Rec.* **259**, 248–262 (2000).
7. J. Männer, On rotation, torsion, lateralization, and handedness of the embryonic heart loop: New insights from a simulation model for the heart loop of chick embryos. *Anat. Rec.* **278A**, 481–492 (2004).
8. J. Männer, The anatomy of cardiac looping: A step towards the understanding of the morphogenesis of several forms of congenital cardiac malformations. *Clinical Anatomy* **22**, 21–35 (2009).
9. F. Tessadori, E. Tsingos, E. S. Colizzi, F. Kruse, S. C. Van Den Brink, M. Van Den Boogaard, V. M. Christoffels, R. M. Merks, J. Bakkers, Twisting of the zebrafish heart tube during cardiac looping is a *tbx5*-dependent and tissue-intrinsic process. *eLife* **10**, e61733 (2021).

10. K. Ivanovitch, I. Esteban, M. Torres, Growth and Morphogenesis during Early Heart Development in Amniotes. *JCDD* **4**, 20 (2017).
11. A. F. M. Moorman, V. M. Christoffels, Cardiac Chamber Formation: Development, Genes, and Evolution. *Physiological Reviews* **83**, 1223–1267 (2003).
12. L. A. Taber, Biophysical mechanisms of cardiac looping. *Int. J. Dev. Biol.* **50**, 323–332 (2006).
13. B. Jensen, T. Wang, V. M. Christoffels, A. F. M. Moorman, Evolution and development of the building plan of the vertebrate heart. *Biochimica et Biophysica Acta* **1833**, 783–794 (2013).
14. N. C. Chi, R. M. Shaw, B. Jungblut, J. Huisken, T. Ferrer, R. Arnaout, I. Scott, D. Beis, T. Xiao, H. Baier, L. Y. Jan, M. Tristani-Firouzi, D. Y. R. Stainier, Genetic and Physiologic Dissection of the Vertebrate Cardiac Conduction System. *PLoS Biol.* **6**, e109 (2008).
15. D. Panáková, A. A. Werdich, C. A. MacRae, Wnt11 patterns a myocardial electrical gradient through regulation of the L-type Ca2+ channel. *Nature* **466**, 874–878 (2010).
16. M. Weber, N. Scherf, A. M. Meyer, D. Panáková, P. Kohl, J. Huisken, Cell-accurate optical mapping across the entire developing heart. *eLife* **6**, e28307 (2017).
17. M. S. Rana, N. C. A. Horsten, S. Tesink-Taekema, W. H. Lamers, A. F. M. Moorman, M. J. B. Van Den Hoff, Trabeculated Right Ventricular Free Wall in the Chicken Heart Forms by Ventricularization of the Myocardium Initially Forming the Outflow Tract. *Circulation Research* **100**, 1000–1007 (2007).
18. J. Liu, M. Bressan, D. Hassel, J. Huisken, D. Staudt, K. Kikuchi, K. D. Poss, T. Mikawa, D. Y. R. Stainier, A dual role for ErbB2 signaling in cardiac trabeculation. *Development* **137**, 3867–3875 (2010).
19. C. Peshkovsky, R. Totong, D. Yelon, Dependence of cardiac trabeculation on neuregulin signaling and blood flow in zebrafish. *Developmental Dynamics* **240**, 446–456 (2011).
20. E. A. Zamir, V. Srinivasan, R. Perucchio, L. A. Taber, Mechanical Asymmetry in the Embryonic Chick Heart During Looping. *Annals of Biomedical Engineering* **31**, 1327–1336 (2003).
21. A. T. Soufan, G. Van Den Berg, J. M. Ruijter, P. A. J. De Boer, M. J. B. Van Den Hoff, A. F. M. Moorman, Regionalized Sequence of Myocardial Cell Growth and Proliferation Characterizes Early Chamber Formation. *Circulation Research* **99**, 545–552 (2006).
22. Y. Shi, J. Yao, G. Xu, L. A. Taber, Bending of the Looping Heart: Differential Growth Revisited. *Journal of Biomechanical Engineering* **136**, 081002 (2014).

23. N. Kawahira, D. Ohtsuka, N. Kida, K. Hironaka, Y. Morishita, Quantitative Analysis of 3D Tissue Deformation Reveals Key Cellular Mechanism Associated with Initial Heart Looping. *Cell Reports* **30**, 3889–3903 (2020).
24. F. J. Manasek, M. B. Burnside, R. E. Waterman, Myocardial cell shape change as a mechanism of embryonic heart looping. *Developmental Biology* **29**, 349–371 (1972).
25. H. J. Auman, H. Coleman, H. E. Riley, F. Olale, H.-J. Tsai, D. Yelon, Functional Modulation of Cardiac Form through Regionally Confined Cell Shape Changes. *PLoS Biol.* **5**, e53 (2007).
26. J. Yang, X. Xu, *α* -Actinin2 is required for the lateral alignment of *Z* discs and ventricular chamber enlargement during zebrafish cardiogenesis. *FASEB j.* **26**, 4230–4242 (2012).
27. P. Choudhry, N. S. Trede, DiGeorge Syndrome Gene *tbx1* Functions through *wnt11r* to Regulate Heart Looping and Differentiation. *PLoS ONE* **8**, e58145 (2013).
28. E. Guzzolino, M. Pellegrino, N. Ahuja, D. Garrity, R. D'Aurizio, M. Groth, M. Baumgart, C. J. Hatcher, A. Mercatanti, M. Evangelista, C. Ippolito, E. Tognoni, R. Fukuda, V. Lionetti, M. Pellegrini, F. Cremisi, L. Pitto, miR-182-5p is an evolutionarily conserved Tbx5 effector that impacts cardiac development and electrical activity in zebrafish. *Cell. Mol. Life Sci.* **77**, 3215–3229 (2020).
29. R. Halabi, P. B. Cechmanek, C. L. Hehr, S. McFarlane, Semaphorin3f as a cardiomyocyte derived regulator of heart chamber development. *Cell Commun. Signal.* **20**, 126 (2022).
30. H. J. Auman, I. H. Fernandes, C. A. Berríos-Otero, S. Colombo, D. Yelon, Zebrafish *smarcc1a* mutants reveal requirements for BAF chromatin remodeling complexes in distinguishing the atrioventricular canal from the cardiac chambers. *Developmental Dynamics* **253**, 157–172 (2024).
31. H. G. Yevick, P. W. Miller, J. Dunkel, A. C. Martin, Structural Redundancy in Supracellular Actomyosin Networks Enables Robust Tissue Folding. *Developmental Cell* **50**, 586–598 (2019).
32. R. Priya, S. Allanki, A. Gentile, S. Mansingh, V. Uribe, H.-M. Maischein, D. Y. R. Stainier, Tension heterogeneity directs form and fate to pattern the myocardial wall. *Nature* **588**, 130–134 (2020).
33. D. C. Deacon, K. R. Nevis, T. J. Cashman, Y. Zhou, L. Zhao, D. Washko, B. Guner-Ataman, C. G. Burns, C. E. Burns, The miR-143-*adducin3* pathway is essential for cardiac chamber morphogenesis. *Development* **137**, 1887–1896 (2010).

34. N. Itasaki, H. Nakamura, M. Yasuda, Changes in the arrangement of actin bundles during heart looping in the chick embryo. *Anat. Embryol.* **180**, 413–420 (1989).
35. I. Shiraishi, T. Takamatsu, T. Minamikawa, S. Fujita, 3-D observation of actin filaments during cardiac myofibrinogenesis in chick embryo using a confocal laser scanning microscope. *Anat. Embryol.* **185**, 401–408 (1992).
36. N. Itasaki, H. Nakamura, H. Sumida, M. Yasuda, Actin bundles on the right side in the caudal part of the heart tube play a role in dextro-looping in the embryonic chick heart. *Anat. Embryol.* **183**, 29–39 (1991).
37. K. S. Latacha, M. C. Rémond, A. Ramasubramanian, A. Y. Chen, E. L. Elson, L. A. Taber, Role of actin polymerization in bending of the early heart tube. *Developmental Dynamics* **233**, 1272–1286 (2005).
38. E. S. Noël, M. Verhoeven, A. K. Lagendijk, F. Tessadori, K. Smith, S. Choorapoikayil, J. Den Hertog, J. Bakkers, A Nodal-independent and tissue-intrinsic mechanism controls heart-looping chirality. *Nat. Commun.* **4**, 2754 (2013).
39. D. A. Voronov, P. W. Alford, G. Xu, L. A. Taber, The role of mechanical forces in dextral rotation during cardiac looping in the chick embryo. *Developmental Biology* **272**, 339–350 (2004).
40. S. Goenezen, M. Y. Rennie, S. Rugonyi, Biomechanics of early cardiac development. *Biomech. Model. Mechanobiol.* **11**, 1187–1204 (2012).
41. S. E. Lindsey, J. T. Butcher, H. C. Yalcin, Mechanical regulation of cardiac development. *Front. Physiol.* **5**, 318 (2014).
42. A. P. Voorhees, H. Han, Biomechanics of Cardiac Function. *Compr. Physiol*, 1623–1644 (2015).
43. J.-F. Le Garrec, J. N. Domínguez, A. Desgrange, K. D. Ivanovitch, E. Raphaël, J. A. Bangham, M. Torres, E. Coen, T. J. Mohun, S. M. Meilhac, A predictive model of asymmetric morphogenesis from 3D reconstructions of mouse heart looping dynamics. *eLife* **6**, e28951 (2017).
44. T. G. R. Andrews, R. Priya, The Mechanics of Building Functional Organs. *Cold Spring Harb. Perspect. Biol.*, a041520 (2024).
45. D. W. Staudt, J. Liu, K. S. Thorn, N. Stuurman, M. Liebling, D. Y. R. Stainier, High-resolution imaging of cardiomyocyte behavior reveals two distinct steps in ventricular trabeculation. *Development* **141**, 585–593 (2014).

46. J. Lee, P. Fei, R. R. S. Packard, H. Kang, H. Xu, K. I. Baek, N. Jen, J. Chen, H. Yen, C.-C. J. Kuo, N. C. Chi, C.-M. Ho, R. Li, T. K. Hsiai, 4-Dimensional light-sheet microscopy to elucidate shear stress modulation of cardiac trabeculation. *Journal of Clinical Investigation* **126**, 1679–1690 (2016).

47. J. R. Hove, R. W. Köster, A. S. Forouhar, G. Acevedo-Bolton, S. E. Fraser, M. Gharib, Intracardiac fluid forces are an essential epigenetic factor for embryonic cardiogenesis. *Nature* **421**, 172–177 (2003).

48. T. Bartman, E. C. Walsh, K.-K. Wen, M. McKane, J. Ren, J. Alexander, P. A. Rubenstein, D. Y. R. Stainier, Early Myocardial Function Affects Endocardial Cushion Development in Zebrafish. *PLoS Biol.* **2**, e129 (2004).

49. J. Vermot, A. S. Forouhar, M. Liebling, D. Wu, D. Plummer, M. Gharib, S. E. Fraser, Reversing Blood Flows Act through *klf2a* to Ensure Normal Valvulogenesis in the Developing Heart. *PLoS Biol.* **7**, e1000246 (2009).

50. B. G. Bruneau, G. Nemer, J. P. Schmitt, F. Charron, L. Robitaille, S. Caron, D. A. Conner, M. Gessler, M. Nemer, C. E. Seidman, J. G. Seidman, A Murine Model of Holt-Oram Syndrome Defines Roles of the T-Box Transcription Factor Tbx5 in Cardiogenesis and Disease. *Cell* **106**, 709–721 (2001).

51. Y. Hiroi, S. Kudoh, K. Monzen, Y. Ikeda, Y. Yazaki, R. Nagai, I. Komuro, Tbx5 associates with Nkx2-5 and synergistically promotes cardiomyocyte differentiation. *Nat. Genet.* **28**, 276–280 (2001).

52. P. E. M. H. Habets, A. F. M. Moorman, D. E. W. Clout, M. A. Van Roon, M. Lingbeek, M. Van Lohuizen, M. Campione, V. M. Christoffels, Cooperative action of Tbx2 and Nkx2.5 inhibits ANF expression in the atrioventricular canal: implications for cardiac chamber formation. *Genes Dev.* **16**, 1234–1246 (2002).

53. V. M. Christoffels, W. M. H. Hoogaars, A. Tessari, D. E. W. Clout, A. F. M. Moorman, M. Campione, T-box transcription factor Tbx2 represses differentiation and formation of the cardiac chambers. *Developmental Dynamics* **229**, 763–770 (2004).

54. Z. Harrelson, R. G. Kelly, S. N. Goldin, J. J. Gibson-Brown, R. J. Bollag, L. M. Silver, V. E. Papaioannou, Tbx2 is essential for patterning the atrioventricular canal and for morphogenesis of the outflow tract during heart development. *Development* **131**, 5041–5052 (2004).

55. A. He, S. W. Kong, Q. Ma, W. T. Pu, Co-occupancy by multiple cardiac transcription factors identifies transcriptional enhancers active in heart. *Proc. Natl. Acad. Sci. U.S.A.* **108**, 5632–5637 (2011).

56. A. Sedletcaia, T. Evans, Heart chamber size in zebrafish is regulated redundantly by duplicated *tbx2* genes. *Developmental Dynamics* **240**, 1548–1557 (2011).

57. D. R. Grassini, A. K. Lagendijk, J. E. De Angelis, J. Da Silva, A. Jeanes, N. Zettler, N. I. Bower, B. M. Hogan, K. A. Smith, Nppa and Nppb act redundantly during zebrafish cardiac development to confine AVC marker expression and reduce cardiac jelly volume. *Development* **145**, dev160739 (2018).

58. C. Guijarro, S. Song, B. Aigouy, R. Clément, P. Villoutreix, R. G. Kelly, Single-cell morphometrics reveals T-box gene-dependent patterns of epithelial tension in the Second Heart field. *Nat. Commun.* **15**, 9512 (2024).

59. V. M. Christoffels, P. E. M. H. Habets, D. Franco, M. Campione, F. De Jong, W. H. Lamers, Z.-Z. Bao, S. Palmer, C. Biben, R. P. Harvey, A. F. M. Moorman, Chamber Formation and Morphogenesis in the Developing Mammalian Heart. *Developmental Biology* **223**, 266–278 (2000).

60. S. B. Burkhard, J. Bakkers, Spatially resolved RNA-sequencing of the embryonic heart identifies a role for Wnt/β-catenin signaling in autonomic control of heart rate. *eLife* **7**, e31515 (2018).

61. A. M. Merks, M. Swinarski, A. M. Meyer, N. V. Müller, I. Özcan, S. Donat, A. Burger, S. Gilbert, C. Mosimann, S. Abdelilah-Seyfried, D. Panáková, Planar cell polarity signalling coordinates heart tube remodelling through tissue-scale polarisation of actomyosin activity. *Nat. Commun.* **9**, 2161 (2018).

62. D. R. Grassini, J. Da Silva, T. E. Hall, G. J. Baillie, C. Simons, R. G. Parton, B. M. Hogan, K. A. Smith, Myosin Vb is required for correct trafficking of N-cadherin and cardiac chamber ballooning. *Developmental Dynamics* **248**, 284–295 (2019).

63. P. C. Bridgman, S. Dave, C. F. Asnes, A. N. Tullio, R. S. Adelstein, Myosin IIB Is Required for Growth Cone Motility. *J. Neurosci.* **21**, 6159–6169 (2001).

64. G. Laevsky, D. A. Knecht, Cross-linking of actin filaments by myosin II is a major contributor to cortical integrity and cell motility in restrictive environments. *Journal of Cell Science* **116**, 3761–3770 (2003).

65. Y. Cai, O. Rossier, N. C. Gauthier, N. Biais, M.-A. Fardin, X. Zhang, L. W. Miller, B. Ladoux, V. W. Cornish, M. P. Sheetz, Cytoskeletal coherence requires myosin-IIA contractility. *Journal of Cell Science* **123**, 413–423 (2010).

66. T. S. Matsui, R. Kaunas, M. Kanzaki, M. Sato, S. Deguchi, Non-muscle myosin II induces disassembly of actin stress fibres independently of myosin light chain dephosphorylation. *Interface Focus.* **1**, 754–766 (2011).

67. C. A. Wilson, M. A. Tsuchida, G. M. Allen, E. L. Barnhart, K. T. Applegate, P. T. Yam, L. Ji, K. Keren, G. Danuser, J. A. Theriot, Myosin II contributes to cell-scale actin network treadmilling through network disassembly. *Nature* **465**, 373–377 (2010).

68. W. Huang, T. S. Matsui, T. Saito, M. Kuragano, M. Takahashi, T. Kawahara, M. Sato, S. Deguchi, Mechanosensitive myosin II but not cofilin primarily contributes to cyclic cell stretch-induced selective disassembly of actin stress fibers. *American Journal of Physiology-Cell Physiology* **320**, C1153–C1163 (2021).

69. M. Zhou, Y.-L. Wang, Distinct Pathways for the Early Recruitment of Myosin II and Actin to the Cytokinetic Furrow. *MBoC* **19**, 318–326 (2008).

70. K. Murthy, P. Wadsworth, Myosin-II-Dependent Localization and Dynamics of F-Actin during Cytokinesis. *Current Biology* **15**, 724–731 (2005).

71. S. Yamashiro, S. Tanaka, L. M. McMillen, D. Taniguchi, D. Vavylonis, N. Watanabe, Myosin-dependent actin stabilization as revealed by single-molecule imaging of actin turnover. *MBoC* **29**, 1941–1947 (2018).

72. E. Berdougo, H. Coleman, D. H. Lee, D. Y. R. Stainier, D. Yelon, Mutation of *weak atrium/atrial myosin heavy chain* disrupts atrial function and influences ventricular morphogenesis in zebrafish. *Development* **130**, 6121–6129 (2003).

73. D. M. Garrity, S. Childs, M. C. Fishman, The *heartstrings* mutation in zebrafish causes heart/fin Tbx5 deficiency syndrome. *Development* **129**, 4635–4645 (2002).

74. M. Albu, E. Affolter, A. Gentile, Y. Xu, K. Kikhi, S. Howard, C. Kuenne, R. Priya, F. Gunawan, D. Y. R. Stainier, Distinct mechanisms regulate ventricular and atrial chamber wall formation. *Nat. Commun.* **15**, 8159 (2024).

75. S. Bisi, A. Disanza, C. Malinverno, E. Frittoli, A. Palamidessi, G. Scita, Membrane and actin dynamics interplay at lamellipodia leading edge. *Current Opinion in Cell Biology* **25**, 565–573 (2013).

76. M. Innocenti, New insights into the formation and the function of lamellipodia and ruffles in mesenchymal cell migration. *Cell Adhesion & Migration* **12**, 401–416 (2018).
77. M. Schaks, G. Giannone, K. Rottner, Actin dynamics in cell migration. *Essays in Biochemistry* **63**, 483–495 (2019).
78. J. Sedzinski, E. Hannezo, F. Tu, M. Biro, J. B. Wallingford, Emergence of an Apical Epithelial Cell Surface *in vivo*. *Developmental Cell* **36**, 24–35 (2016).
79. J. Sedzinski, E. Hannezo, F. Tu, M. Biro, J. B. Wallingford, RhoA regulates actin network dynamics during apical surface emergence in multiciliated epithelial cells. *J. Cell Sci.* **130**, 420–428 (2017).
80. C. Santa-Cruz Mateos, A. Valencia-Expósito, I. M. Palacios, M. D. Martín-Bermudo, Integrins regulate epithelial cell shape by controlling the architecture and mechanical properties of basal actomyosin networks. *PLoS Genet.* **16**, e1008717 (2020).
81. S. Li, Z.-Y. Liu, H. Li, S. Zhou, J. Liu, N. Sun, K.-F. Yang, V. Dougados, T. Mangeat, K. Belguise, X.-Q. Feng, Y. Liu, X. Wang, Basal actomyosin pulses expand epithelium coordinating cell flattening and tissue elongation. *Nat. Commun.* **15**, 3000 (2024).
82. Y. Matsuoka, X. Li, V. Bennett, Adducin: structure, function and regulation: *Cell. Mol. Life Sci.* **57**, 884–895 (2000).
83. K. Y. Miyasaka, Y. S. Kida, T. Banjo, Y. Ueki, K. Nagayama, T. Matsumoto, M. Sato, T. Ogura, Heartbeat regulates cardiogenesis by suppressing retinoic acid signaling via expression of *miR-143*. *Mechanisms of Development* **128**, 18–28 (2011).
84. M. C. Rémond, J. A. Fee, E. L. Elson, L. A. Taber, Myosin-based contraction is not necessary for cardiac c-looping in the chick embryo. *Anat. Embryol.* **211**, 443–454 (2006).
85. V. A. Lombardo, M. Heise, M. Moghtadaei, D. Bornhorst, J. Männer, S. Abdelilah-Seyfried, Morphogenetic control of zebrafish cardiac looping by Bmp signaling. *Development* **146**, dev180091 (2019).
86. L. D'Amico, I. C. Scott, B. Jungblut, D. Y. R. Stainier, A Mutation in Zebrafish *hmgcr1b* Reveals a Role for Isoprenoids in Vertebrate Heart-Tube Formation. *Current Biology* **17**, 252–259 (2007).
87. Y.-F. Lin, I. Swinburne, D. Yelon, Multiple influences of blood flow on cardiomyocyte hypertrophy in the embryonic zebrafish heart. *Developmental Biology* **362**, 242–253 (2012).

88. D. M. Leerberg, K. Sano, B. W. Draper, Fibroblast growth factor signaling is required for early somatic gonad development in zebrafish. *PLoS Genet.* **13**, e1006993 (2017).
89. R Core Team, R: A Language and Environment for Statistical Computing., R Foundation for Statistical Computing (2024); https://www.R-project.org/.
90. RStudio Team, RStudio: Integrated Development for R., RStudio, PBC (2024); http://www.rstudio.com/.
91. H. Wickham, R. François, L. Henry, K. Müller, D. Vaughan, dplyr: A Grammar of Data Manipulation, (2023); https://CRAN.R-project.org/package=dplyr.
92. E. Clarke, S. Sherril-Mix, C. Dawson, ggbeeswarm: Categorical Scatter (Violin Point) Plots, (2023); https://CRAN.R-project.org/package=ggbeeswarm.
93. H. Wickham, *Ggplot2: Elegant Graphics for Data Analysis* (Springer-Verlag New York, 2016; https://ggplot2.tidyverse.org).
94. P. Aphalo, ggpmisc: Miscellaneous Extensions to "ggplot2," (2024); https://CRAN.R-project.org/package=ggpmisc.
95. A. Kassambara, ggpubr: "ggplot2" Based Publication Ready Plots, (2023); https://CRAN.R-project.org/package=ggpubr.
96. C. Wilke, B. Wiernik, ggtext: Improved Text Rendering Support for "ggplot2," (2022); https://wilkelab.org/ggtext/.
97. D. Sarkar, *Lattice: Multivariate Data Visualization with R* (Springer New York, New York, NY, 2008; http://lmdvr.r-forge.r-project.org).
98. H. Wickham, The Split-Apply-Combine Strategy for Data Analysis. *Journal of Statistical Software* **40**, 1–29 (2011).
99. H. Wickham, M. Averick, J. Bryan, W. Chang, L. McGowan, R. François, G. Grolemund, A. Hayes, L. Henry, J. Hester, M. Kuhn, T. Pedersen, E. Miller, S. Bache, K. Müller, J. Ooms, D. Robinson, D. Seidel, V. Spinu, K. Takahashi, D. Vaughan, C. Wilke, K. Woo, H. Yutani, Welcome to the Tidyverse. *JOSS* **4**, 1686 (2019).

Figures

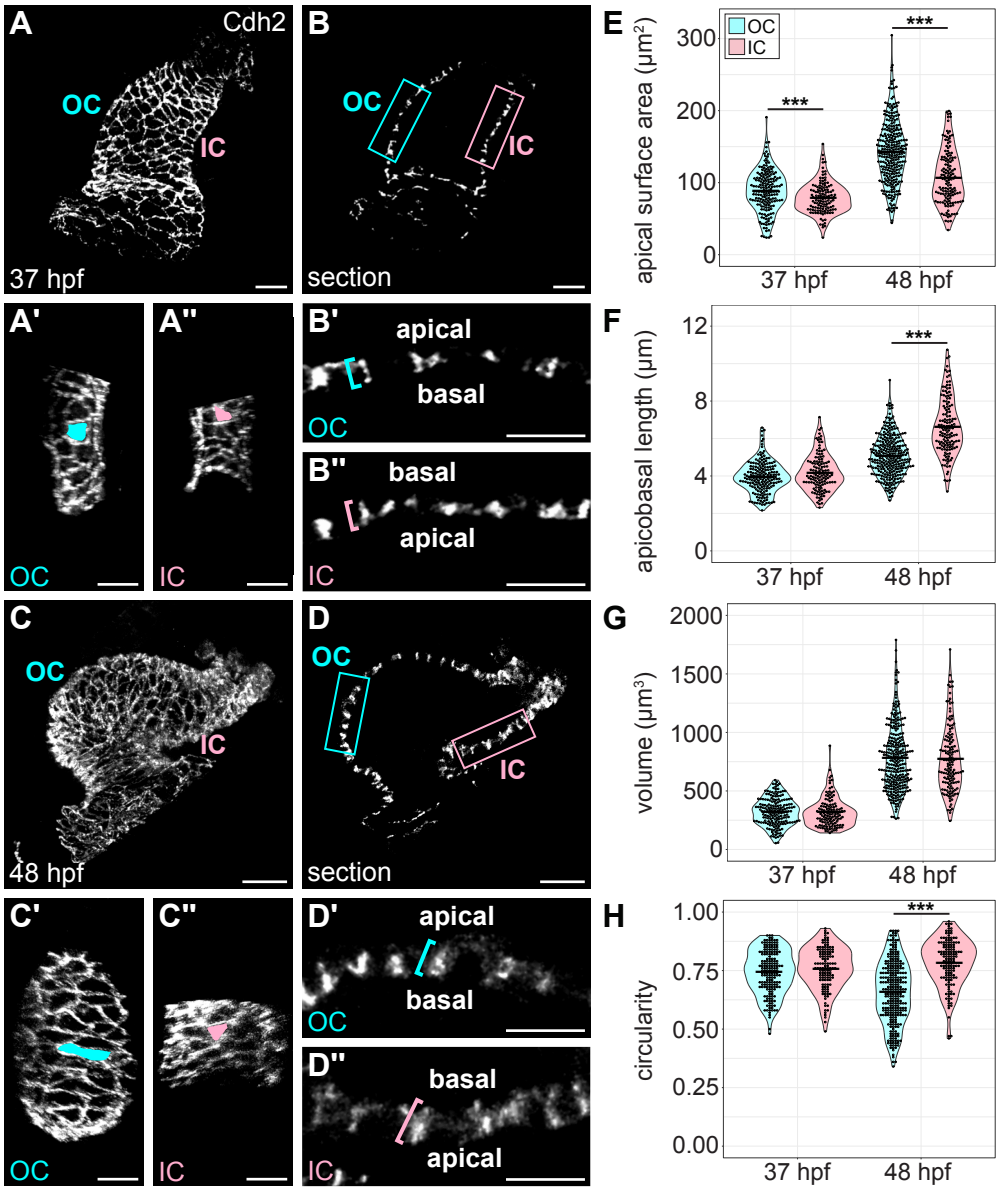

Fig. 1. OC and IC cardiomyocyte morphologies diverge during curvature formation. (**A**, **C**) 3D reconstructions of 37 hpf (A) and 48 hpf (C) wild-type hearts. Immunostaining for Cdh2 labels lateral membranes of cardiomyocytes. OC (A′, C′) and IC (A″, C″) are shown for hearts in (A) and (C), respectively. Apical surface area of an individual cardiomyocyte is illustrated by blue or pink fill. (**B**, **D**) Sections through hearts in (A, C). (B′, B″, D′, D″) are magnified views of blue (OC) and pink (IC) boxed regions in (B, D); blue and pink brackets highlight apicobasal length of individual cardiomyocytes. (**E-H**) Violin plots compare apical surface area, apicobasal length, volume, or circularity of OC and IC cardiomyocytes at 37 and 48 hpf. Each dot represents an individual cell. Volume is calculated as LxWxH; circularity is calculated as $4\pi(A/P^2)$. *** denotes $p < 0.001$, Wilcoxon test. Significance only shown for OC/IC comparisons; all metrics are significantly different between developmental stages of the same region (*i.e.* 37 hpf OC vs 48 hpf OC, and 37 hpf IC vs 48 hpf IC). 37 hpf OC (N=5 embryos, n=183 cells); 37 hpf IC (N=5 embryos, n=127 cells); 48 hpf OC (N=6 embryos, n=281 cells); 48 hpf IC (N=6 embryos, n=143 cells). Scale bars = 30 μm (A, B, C, D); 20 μm (A′, A″, C′, C″); 15 μm (B′, B″, D′, D″).

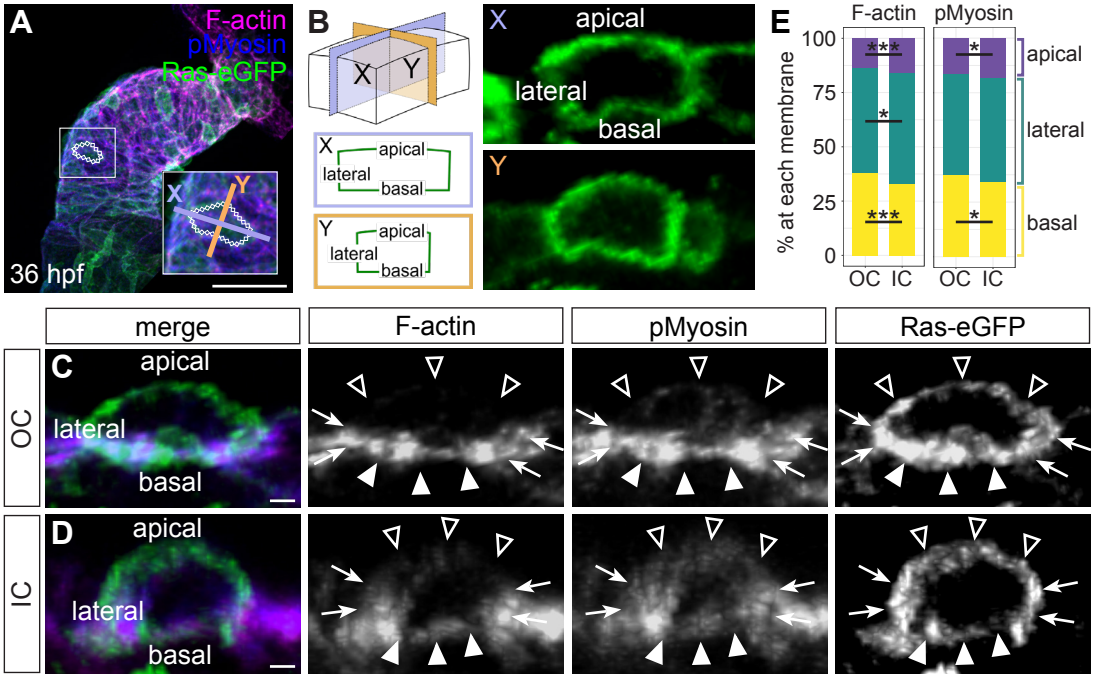

Fig. 2. OC and IC cardiomyocytes exhibit differential localization of subcellular actomyosin during early curvature formation. (**A**) Whole heart from a 36 hpf embryo carrying *Tg(myl7:eGFP-Hsa.HRAS)* (*86*), immunostained for membrane-bound GFP and pMyosin and stained with Phalloidin to label F-actin. Inset magnifies a single cardiomyocyte. (**B**) Visual representation of approach for measuring the percentages of F-actin or pMyosin at each membrane in individual cardiomyocytes. Briefly, each OC or IC cardiomyocyte was bisected in two axes, resulting in two cross-sections for each cell (X, purple; Y, orange). The cell boundaries in X and Y are visible due to eGFP localization to the membranes. In these images, the basal membrane is always at the bottom. (**C**, **D**) Cross-sections through representative individual cardiomyocytes from the OC (C) or IC (D). Empty arrowheads: apical membranes. Filled arrowheads: basal membranes. Arrows: lateral membranes. (**E**) Stacked bar charts showing the mean percentage of F-actin or pMyosin at each membrane. * denotes $p < 0.05$ and *** denotes $p < 0.001$, Wilcoxon test. OC (N=7 embryos, n=199 cells); IC (N=7 embryos, n=123 cells). Scale bars = 50 µm (A); 2 µm (C,D).

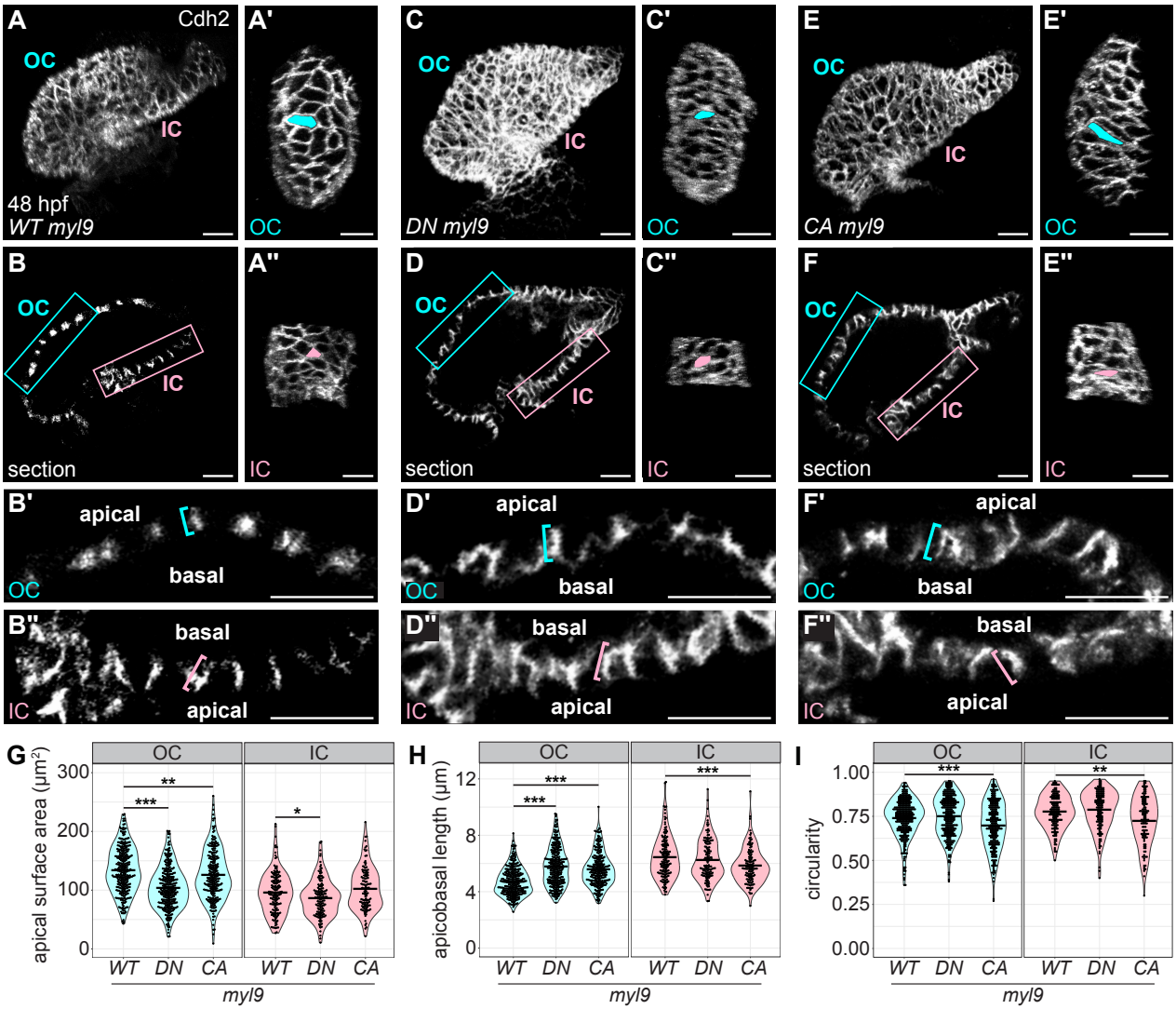

Fig. 3. Tissue-specific modulation of NMII activity dampens the divergence of OC and IC cardiomyocyte morphologies. (**A**, **C**, **E**) 3D reconstructions of 48 hpf hearts expressing *Tg(myl7:WT-myl9-mScarlet)* (A), *Tg(myl7:DN-myl9-eGFP)* (C), or *Tg(myl7:CA-myl9-eGFP)* (E). Immunostaining for Cdh2 labels lateral membranes of cardiomyocytes. OCs (A′, C′, E′) and ICs (A″, C″, E″) are shown for hearts in (A, C, E). Apical surface area of an individual cardiomyocyte is illustrated by blue or pink fill. (**B**, **D**, **F**) Sections through hearts in (A,C,E). (B′ ,B″, D′, D″, F′, F″) are magnified views of blue (OC) and pink (IC) boxed regions in (B, D, F); blue and pink brackets highlight apicobasal length of individual cardiomyocytes. (**G-I**) Violin plots compare apical surface area, apicobasal length, or circularity of cardiomyocytes between embryos expressing the different transgenes, split by curvature. Circularity is calculated as $4\pi(A/P^2)$. Each dot represents an individual cell. * denotes $p < 0.05$, ** denotes $p < 0.01$, and *** denotes $p < 0.001$, Wilcoxon test. *Tg(myl7:WT-myl9-mScarlet)* OC (N=6 embryos, n=308 cells); *Tg(myl7:WT-myl9-mScarlet)* IC (N=6 embryos, n=159 cells); *Tg(myl7:DN-myl9-eGFP)* OC (N=6 embryos, n=298 cells); *Tg(myl7:DN-myl9-eGFP)* IC (N=6 embryos, n=143 cells); *Tg(myl7:CA-myl9-eGFP)* OC (N=6 embryos, n=253 cells); *Tg(myl7:CA-myl9-eGFP)* IC (N=6 embryos, n=123 cells). Scale bars = 20 μm.

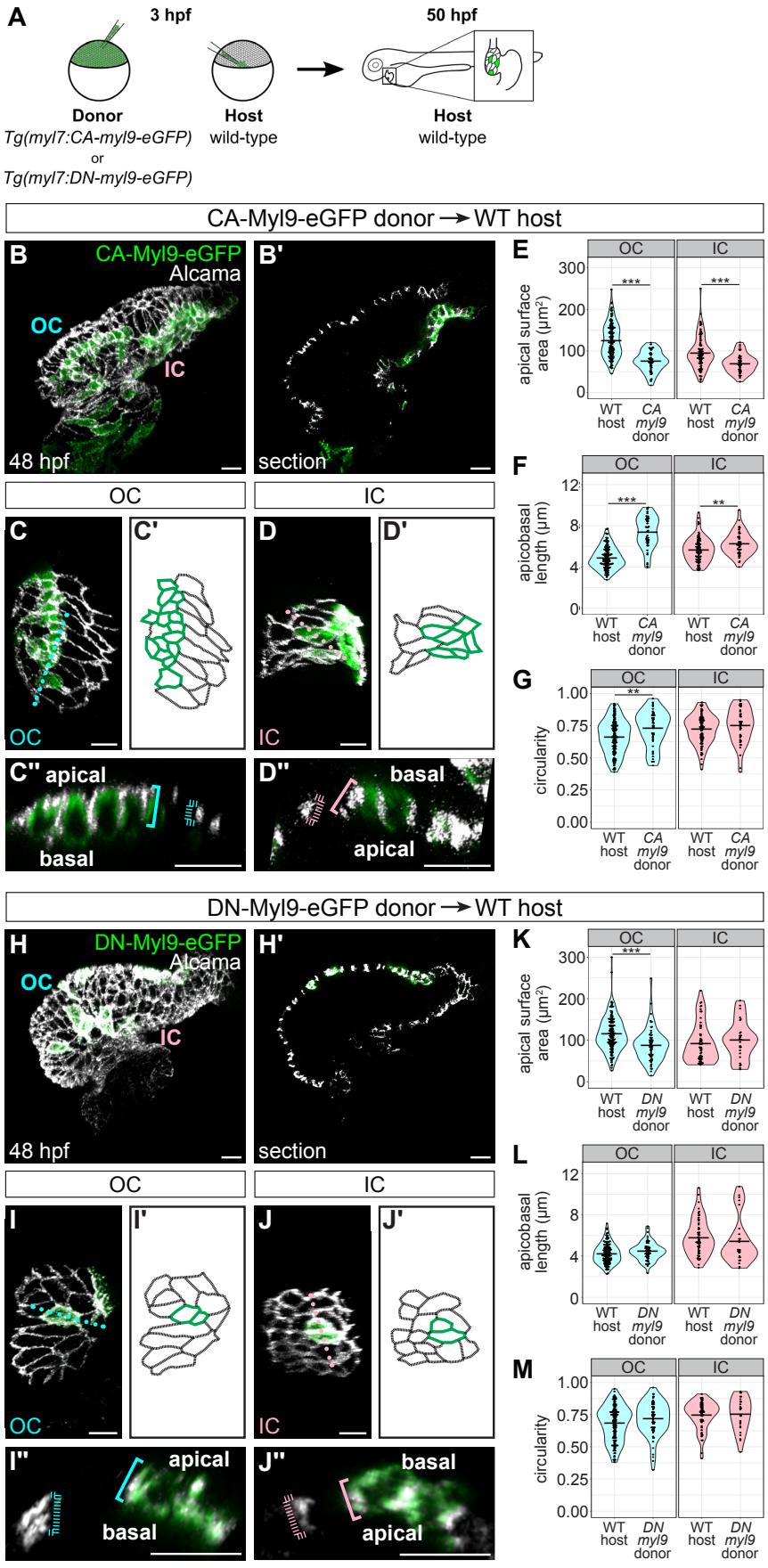

Fig. 4. Cell-intrinsic modulation of NMII activity alters cardiomyocyte shape. (**A**) Schematic of blastomere transplantation experiment. (**B**, **H**) 3D reconstructions of 48 hpf wild-type (WT) host hearts containing donor-derived cardiomyocytes expressing *Tg(myl7:CA-myl9-eGFP)* (B) or *Tg(myl7:DN-myl9-eGFP)* (H); immunostaining for Alcama labels lateral membranes of cardiomyocytes. (B′, H′) Sections through hearts in (B, H). OC (**C**, **I**) and IC (**D**, **J**) are shown from additional mosaic hearts other than those in (B, H). (C′, D′, I′, J′) Tracings of the cardiomyocytes in (C, D, I, J). Green outlines indicate donor-derived cardiomyocytes; black outlines indicate host-derived cardiomyocytes. (C″, D″, I″, J″) Cross-sections through positions indicated by dotted lines in (C, D, I, J). Blue and pink brackets highlight apicobasal length of individual cardiomyocytes, with dashed brackets for host-derived cardiomyocytes and solid brackets for donor-derived cardiomyocytes. (**E-G**, **K-M**) Violin plots compare apical surface area, apicobasal length, and circularity of host-derived cardiomyocytes to those of donor-derived cardiomyocytes. Each dot represents an individual cell. ** denotes $p < 0.01$ and *** denotes $p < 0.001$, Wilcoxon test. For *Tg(myl7:CA-myl9-eGFP)* into WT transplants: host OC (N=5 embryos, n=145 cells); donor OC (N=8 embryos, n=49 cells); host IC (N=7 embryos, n=91 cells); donor IC (N=7 embryos, n=44 cells). For *Tg(myl7:DN-myl9-eGFP)* into WT transplants: host OC (N=10 embryos, n=156 cells); donor OC (N=10 embryos, n=65 cells); host IC (N=8 embryos, n=60 cells); donor IC (N=8 embryos, n=27 cells). Scale bars = 15 μm.

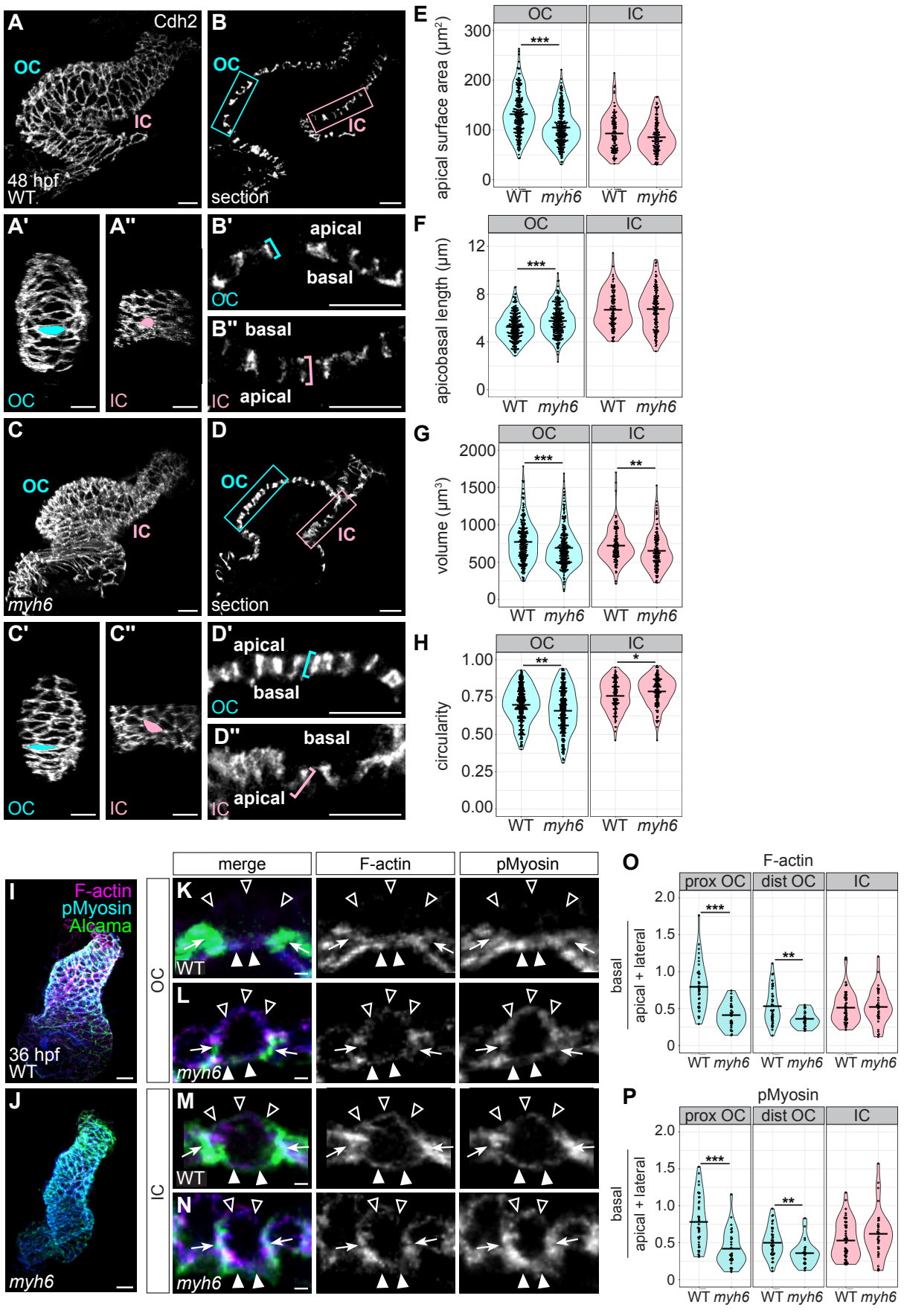

Fig. 5. Reduced blood flow inhibits the divergence of OC and IC cardiomyocyte shapes and actomyosin organization. (A-H) Comparison of cardiomyocyte morphologies in wild-type and *myh6* mutant hearts. (**A**, **C**) 3D reconstructions of wild-type (A) and *myh6* mutant (C) hearts at 48 hpf; immunostaining for Cdh2 labels lateral membranes of cardiomyocytes. OCs (A′, C′) and ICs (A″, C″) are shown for hearts in (A, C). Apical surface area of an individual cardiomyocyte is illustrated by blue or pink fill. (**B**, **D**) Sections through hearts in (A, C). (B′, B″, D′, D″) Magnified views of blue (OC) and pink (IC) boxed regions in (B, D); blue and pink brackets highlight apicobasal length of individual cells. (**E-H**) Violin plots compare apical surface area, apicobasal length, volume, and circularity for cells from wild-type and *myh6* mutant hearts. Each dot represents an individual cell. (H) Note that *myh6* OC cardiomyocytes are more elongated than wild-type OC cardiomyocytes, a finding that contrasts with our previous work (*25*). We posit that this discrepancy could arise from changes in the genetic background over time or to differences in how data were collected (*e.g.* where the OC boundary was drawn or how data for individual cardiomyocytes were collected). (I-P) Comparison of subcellular actomyosin organization in wild-type and *myh6* mutant cardiomyocytes. (**I**, **J**) Wild-type (I) and *myh6* mutant (J) hearts at 36 hpf, immunostained for pMyosin and stained with Phalloidin to label F-actin. Immunostaining for Alcama labels lateral membranes of cardiomyocytes. (**K-N**) Cross-sections through representative cardiomyocytes from the OC (K, L) and IC (M, N) of 36 hpf wild-type (K, M) and *myh6* mutant (L, N) hearts. Empty arrowheads: apical membranes. Filled arrowheads: basal membranes. Arrows: lateral membranes. (**O**) Violin plots show calculated values of (mean basal F-actin / (mean apical F-actin + mean lateral F-actin)) for individual cells. (**P**) Violin plots of calculated values as in (O), but for pMyosin. For all violin plots, * denotes $p < 0.05$, ** denotes $p < 0.01$, and *** denotes $p < 0.001$, Wilcoxon test. For morphometrics: wild-type OC (N=5 embryos, 267 cells); *myh6* OC (N=6 embryos, n=275 cells); wild-type IC (N=5 embryos, n=120 cells); *myh6* IC (N=6 embryos, n=135 cells). For actomyosin localization: wild-type proximal OC (N=5 embryos, n=39 cells); *myh6* proximal OC (N=4 embryos, n=32 cells); wild-type distal OC (N=5 embryos, n=41 cells); *myh6* distal OC (N=4 embryos, n=24 cells); wild-type IC (N=5 embryos, n=54 cells); *myh6* IC (N=4 embryos, n=35 cells). Scale bars = 20 μm (A-D, I, J); 2 μm (K-N).

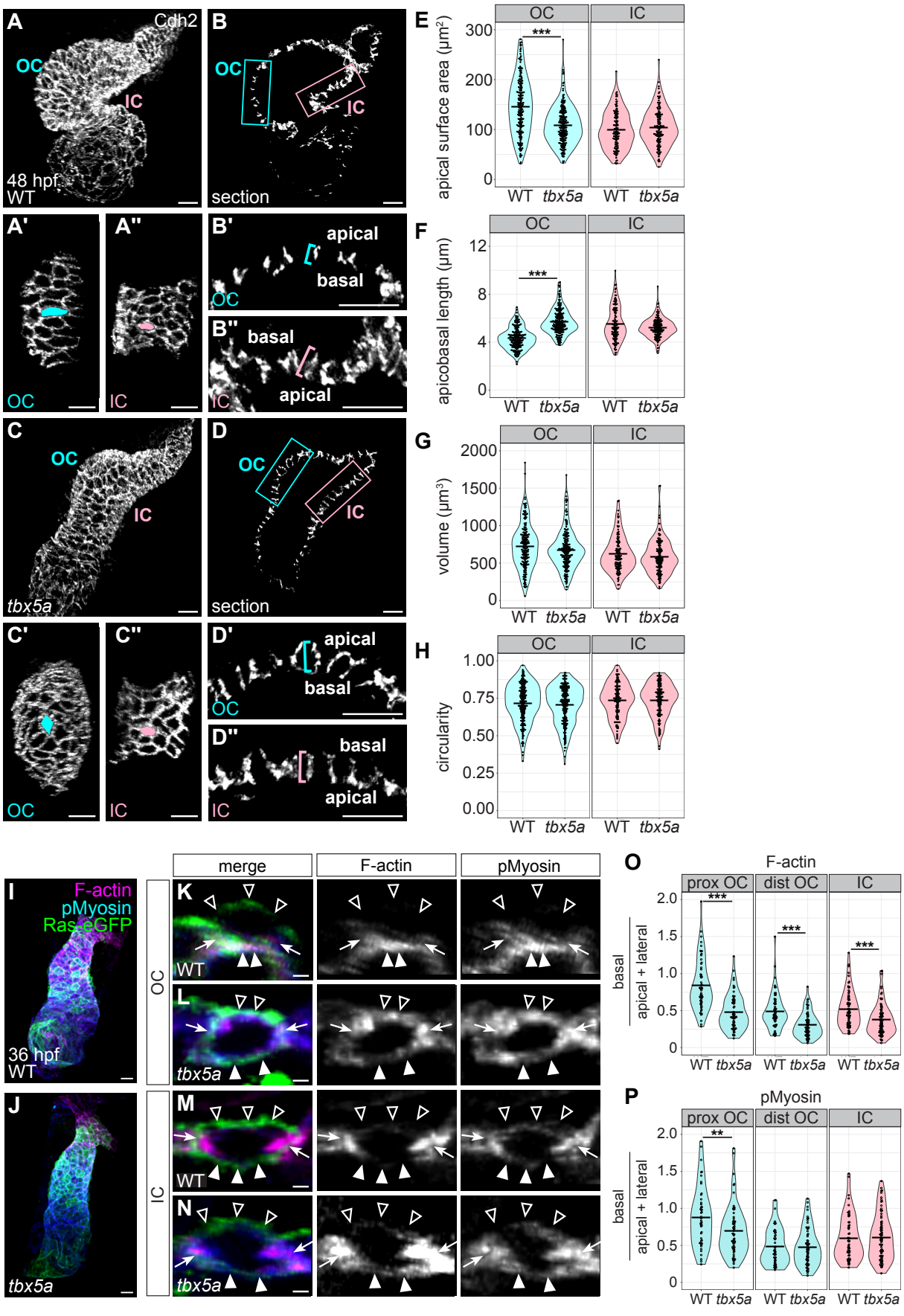

Fig. 6. *tbx5a* regulates pathways that support the divergence of OC and IC cardiomyocyte morphologies and actomyosin organization. (A-H) Comparison of cardiomyocyte morphologies in wild-type and *tbx5a* mutant hearts. (**A**, **C**) 3D reconstructions of wild-type (A) and *tbx5a* mutant (C) hearts at 48 hpf; immunostaining for Cdh2 labels lateral membranes of cardiomyocytes. OCs (A′, C′) and ICs (A″, C″) are shown for hearts in (A, C). Apical surface area of an individual cardiomyocyte is illustrated by blue or pink fill. (**B**, **D**) Sections through hearts in (A, C). (B′, B″, D′, D″) Magnified views of blue (OC) and pink (IC) boxed regions in (B, D); blue and pink brackets highlight apicobasal length of individual cardiomyocytes. (**E-H**) Violin plots compare apical surface area, apicobasal length, volume, and circularity for cardiomyocytes from wild-type and *tbx5a* mutant hearts. Each dot represents an individual cell. (I-P) Comparison of subcellular actomyosin organization in wild-type and *tbx5a* mutant cardiomyocytes. (**I, J**) Wild-type (I) and *tbx5a* mutant (J) hearts at 36 hpf, immunostained for membrane-bound eGFP and pMyosin, and stained with Phalloidin to label F-actin. (**K-N**) Cross-sections through representative cardiomyocytes from the OC (K, L) and IC (M, N) of 36 hpf wild-type (K, M) and *tbx5a* mutant (L, N) hearts. Empty arrowheads: apical membranes. Filled arrowheads: basal membranes. Arrows: lateral membranes. (**O**) Violin plots show calculated values of (mean basal F-actin / (mean apical F-actin + mean lateral F-actin)) for individual cells. (**P**) Violin plots of calculated values as in (O), but for pMyosin. For all violin plots, ** denotes $p < 0.01$ and *** denotes $p < 0.001$, Wilcoxon test. For morphometrics: wild-type OC (N=5 embryos, n=214 cells); *tbx5a* OC (N=5 embryos, n=220 cells); wild-type IC (N=5 embryos, n=126 cells); *tbx5a* IC (N=5 embryos, n=141 cells). For actomyosin localization: wild-type proximal OC (N=5 embryos, n=58 cells); *tbx5a* proximal OC (N=5 embryos, n=64 cells); wild-type distal OC (N=5 embryos, n=61 cells); *tbx5a* distal OC (N=5 embryos, n=67 cells); wild-type IC (N=5 embryos, n=69 cells); *tbx5a* IC (N=5 embryos, n=81 cells). Scale bars = 20 μm (A-D, I, J); 2 μm (K-N).

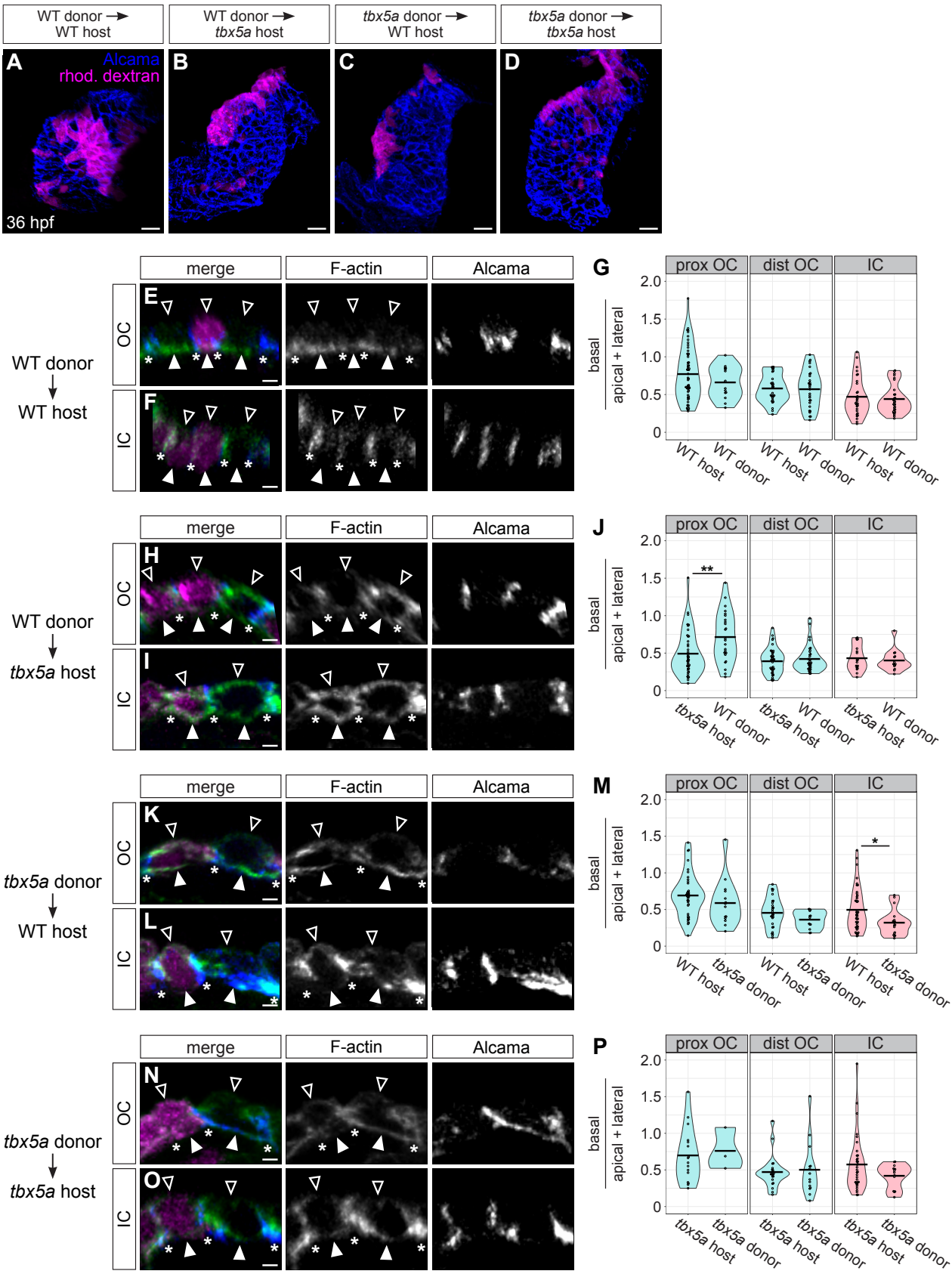

Fig. 7. *tbx5a* functions in a partially cell-autonomous manner to support subcellular F-actin organization. (**A-D**) 3D reconstructions show examples of mosaic 36 hpf hearts resulting from blastomere transplantation. Immunostaining for Alcama labels lateral membranes of cardiomyocytes (blue), and donor-derived cells are labeled with rhodamine-dextran (magenta). (**E**, **F**, **H**, **I**, **K**, **L**, **N**, **O**) Cross-sections through representative cardiomyocytes from the OC (E, H, K, N) and IC (F, I, L, O) from each of the four transplant scenarios. Immunostaining for Alcama labels lateral membranes of cardiomyocytes (blue) and staining with Phalloidin labels F-actin (green); rhodamine dextran labels donor-derived cardiomyocytes (magenta). Empty arrowheads: apical membranes. Filled arrowheads: basal membranes. Asterisks: basal extreme of lateral membranes. (**G**, **J**, **M**, **P**) Violin plots compare calculated values of (mean basal F-actin / (mean apical F-actin + mean lateral F-actin)) of host-derived cardiomyocytes to those of donor-derived cardiomyocytes for each transplant scenario. Each dot represents an individual cell. * denotes $p < 0.05$, and ** denotes $p < 0.01$, Wilcoxon test. For WT into WT transplants: host proximal OC (N=6 embryos, n=55 cells); donor proximal OC (N=7 embryos, n=34 cells); host distal OC (N=5 embryos, n=30 cells); donor distal OC (N=6 embryos, n=29 cells); host IC (N=4 embryos, n=30 cells); donor IC (N=4 embryos, n=29 cells). For WT into *tbx5a* transplants: host proximal OC (N=5 embryos, n=40 cells); donor proximal OC (N=5 embryos, n=25 cells); host distal OC (N=5 embryos, n=40 cells); donor distal OC (N=5 embryos, n=35 cells); host IC (N=5 embryos, n=18 cells); donor IC (N=5 embryos, n=14 cells). For *tbx5a* into WT transplants: host proximal OC (N=7 embryos, n=38 cells); donor proximal OC (N=5 embryos, n=14 cells); host distal OC (N=6 embryos, n=28 cells); donor distal OC (N=5 embryos, n=13 cells); host IC (N=5 embryos, n=44 cells); donor IC (N=5 embryos, n=18 cells). For *tbx5a* into *tbx5a* transplants: host proximal OC (N=4 embryos, n=16 cells); donor proximal OC (N=2 embryos, n=3 cells); host distal OC (N=4 embryos, n=21 cells); donor distal OC (N=4 embryos, n=14 cells); host IC (N=5 embryos, n=36 cells); donor IC (N=5 embryos, n=14 cells). Scale bars = 20 μm (A-D); 3 μm (E, F, H, I, K, L, N, O).

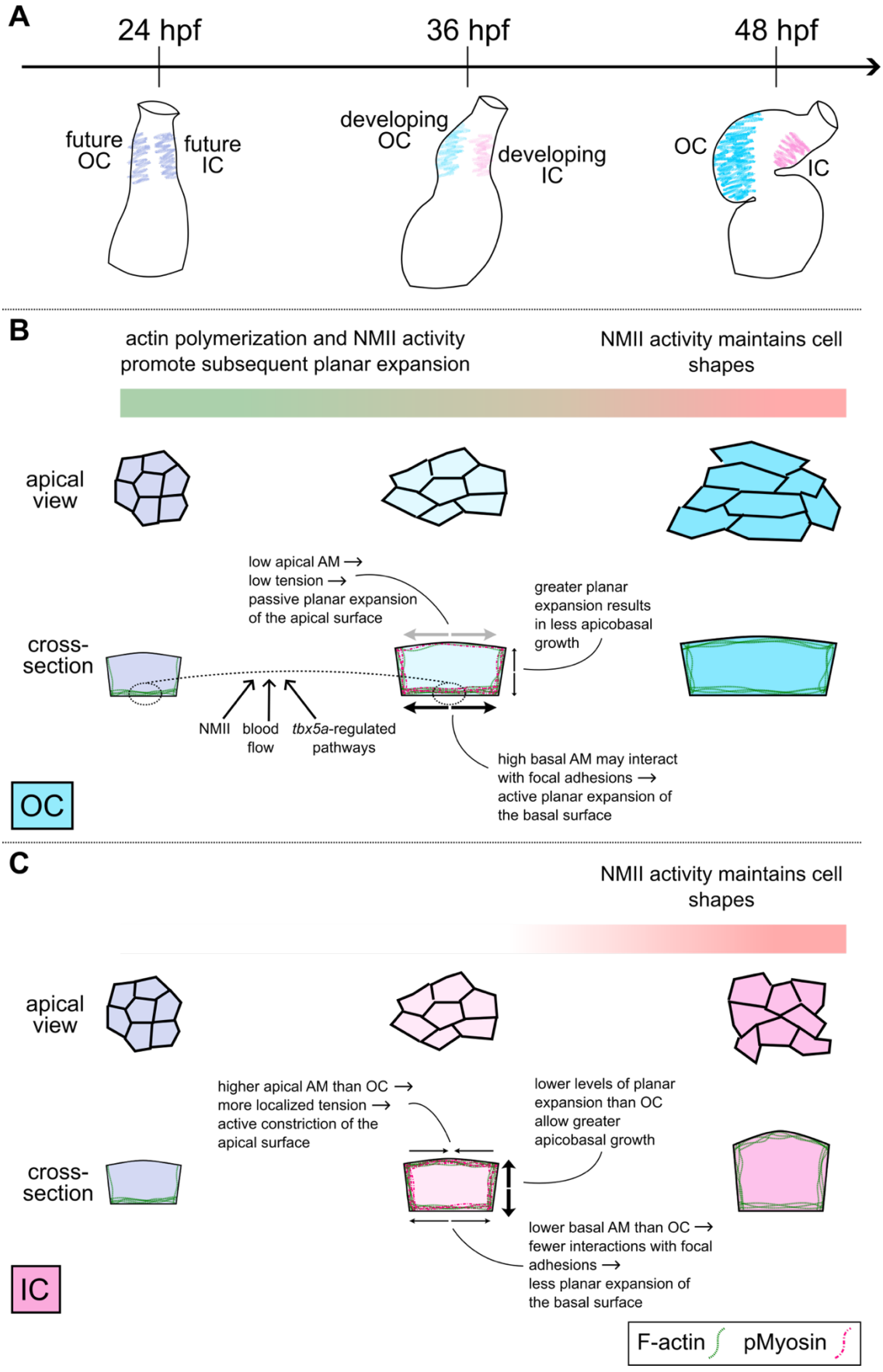

Fig. 8. Changes to the actin cytoskeleton and cardiomyocyte shape during curvature formation. (**A**) During the second day of zebrafish development, the linear heart tube transforms into a two-chambered heart. Once similarly contoured regions (light purple) bend and stretch to become the convex OC (blue) and the concave IC (pink). (**B**, **C**) Schematic portrays select cellular and subcellular traits and events that underlie curvature formation. At the linear heart tube stage, cardiomyocytes in the future OC and IC (particularly those positioned more proximally, as shown here; light purple) present similar morphologies and F-actin organization, with most F-actin restricted to the basal surface. Over the next 12 hours, OC (B, light blue) and IC (C, light pink) cardiomyocytes have begun to diverge slightly in shape, and F-actin organization has also diverged. In the OC, there remains a large pool of basal F-actin, whereas in the IC, a lower proportion of F-actin resides at the basal surface and there instead exists a larger pool of apical and lateral F-actin. This difference is facilitated by NMII activity, as well as by blood flow through the ventricle and by *tbx5a*-regulated pathways; specifically, these factors appear to influence either the retention of basal F-actin or the prevention of formation of F-actin networks at the lateral and apical surfaces in OC cardiomyocytes. We propose that the basal enrichment of F-actin in OC cardiomyocytes (B) allows for interaction with focal adhesions to enact outward pushing of the basal surface (thick black arrows). Simultaneously, maintaining a low amount of actomyosin at the apical surface may allow this surface to passively expand along with the actively spreading basal surface (grey arrows). In the IC (C), we speculate that lower levels of basal F-actin might result in weakened interaction with focal adhesions and less outward pushing (thin black arrows), while more actomyosin at the apical surface may increase tension and prevent passive spreading (inward-facing thin black arrows). As a consequence of limited planar expansion, the increasing volume of IC cardiomyocytes instead leads to expansion along the apicobasal axis (thick black arrows). By 48 hpf, OC (darker blue) and IC (darker pink) cells have acquired strikingly different cell morphologies. In contrast, the actin cytoskeleton seems to have converged into similar arrangements in both OC and IC cardiomyocytes, with F-actin distributed fairly equally around all cell membranes, and, in both regions, it seems that the role of actomyosin changes altogether, with the primary role of NMII being to maintain cell shapes.